

A spectral and photometric study of 102 star forming regions in seven spiral galaxies

A. S. Gusev,¹ F. Sakhibov,² A. E. Piskunov,³ N. V. Kharchenko,⁴ V. V. Bruevich,¹
O. V. Ezhkova,¹ S. A. Guslyakova,⁵ V. Lang,² E. V. Shimanovskaya,¹
and Y. N. Efremov¹

¹ Sternberg Astronomical Institute, Lomonosov Moscow State University, Universitetsky pr. 13, 119992 Moscow, Russia

² University of Applied Sciences of Mittelhessen, Campus Friedberg, Department of Mathematics, Natural Sciences and Data Processing, Wilhelm-Leuschner-Strasse 13, 61169 Friedberg, Germany

³ Institute of Astronomy, Russian Academy of Sciences, ul. Pyatnitskaya 48, 119017 Moscow, Russia

⁴ Main Astronomical Observatory, National Academy of Sciences of Ukraine, ul. Zabolotnogo 27, 03680 Kiev, Ukraine

⁵ Institute for Space Research, Russian Academy of Sciences, ul. Profsoyuznaya 84/32, 117997 Moscow, Russia

Accepted 2016 January 25. Received 2016 January 25; in original form 2015 April 1

ABSTRACT

We present a study of complexes of young massive star clusters (YMCs), embedded in extragalactic giant H II regions, based on the coupling of spectroscopic with photometric and spectrophotometric observations of about 100 star forming regions in seven spiral galaxies (NGC 628, NGC 783, NGC 2336, NGC 6217, NGC 6946, NGC 7331, and NGC 7678). The complete observational database has been observed and accumulated within the framework of our comprehensive study of extragalactic star forming regions. The current paper presents the last part of either unpublished or refreshed photometric and spectrophotometric observations of the galaxies NGC 6217, NGC 6946, NGC 7331, and NGC 7678. We derive extinctions, chemical abundances, continuum and line emissions of ionised gas, ages and masses for cluster complexes. We find the young massive cluster complexes to have ages no greater than 10 Myr and masses between $10^4 M_\odot$ and $10^7 M_\odot$, and the extinctions A_V vary between ~ 0 and 3 mag, while the impact of the nebular emission on integrated broadband photometry mainly is not greater than 40% of the total flux and is comparable with accuracies of dereddened photometric quantities. We also find evidence of differential extinction of stellar and gas emissions in some clusters, which hinders the photometric determination of ages and masses in these cases. Finally, we show that young massive cluster complexes in the studied galaxies and open clusters in the Milky Way form a continuous sequence of luminosities/masses and colour/ages.

Key words: H II regions – galaxies: photometry – galaxies: ISM – galaxies: star clusters – open clusters and associations: general

1 INTRODUCTION

This paper presents the second part of our comprehensive study of star forming (SF) regions in spiral galaxies. The results of spectroscopic observations of 102 H II regions in seven galaxies were presented in the previous papers (Gusev et al. 2012; Gusev, Sakhibov & Dodonov 2013). Here we present the results of *UBVRI* photometry and *H α* spectrophotometry for the same SF regions in the galaxies. We obtained and analyzed *UBVRI* photometric data for 101 out of the 102 studied H II regions in seven galaxies (except object No. 1 in NGC 7331), and *H α* spectrophotometric data for 53 H II regions in galaxies NGC 628, NGC 6946, and NGC 7331. A combination of the multicolour photometry and spectroscopic observations of SF regions provides a clue to the

properties of young massive cluster complexes embedded in giant H II regions in seven spiral galaxies NGC 628 (10), NGC 783 (8), NGC 2336 (28), NGC 6217 (3), NGC 6946 (39), NGC 7331 (3), and NGC 7678 (10). Since we observed both giant H II regions with embedded cluster complexes, and the embedded cluster complexes themselves, we call the studied objects ‘star forming regions’ (SF regions).

A star forming region in a galaxy is a single conglomerate of newly formed star clusters, dust clouds, and ionised gas. Star forming regions have a hierarchical structure over a large range of scales. On small scales, there are young star clusters with diameters of a few parsecs and OB associations with diameters of several tens of parsecs. The largest coherent star formation re-

Table 1. The galaxy sample.

Galaxy	Type	B_i (mag)	M_B^a (mag)	Inclination (degree)	PA (degree)	R_{25}^b (arcmin)	R_{25}^b (kpc)	D (Mpc)	$A(B)_{\text{Gal}}$ (mag)	$A(B)_{\text{in}}$ (mag)	Notes ^c
1	2	3	4	5	6	7	8	9	10	11	12
NGC 628	Sc	9.70	−20.72	7	25	5.23	10.96	7.2	0.254	0.04	1, 2
NGC 783	Sc	13.18	−22.01	43	57	0.71	14.56	70.5	0.222	0.45	3
NGC 2336	SB(R)bc	11.19	−22.14	55	175	2.51	23.51	32.2	0.120	0.41	4
NGC 6217	SB(R)bc	11.89	−20.45	33	162	1.15	6.89	20.6	0.158	0.22	5, 6
NGC 6946	SABc	9.75	−20.68	31	62	7.74	13.28	5.9	1.241	0.04	6
NGC 7331	Sbc	10.20	−21.68	75	169	4.89	20.06	14.1	0.331	0.61	6
NGC 7678	SBC	12.50	−21.55	44	21	1.04	14.46	47.8	0.178	0.23	6, 7

^a Absolute magnitude of a galaxy corrected for Galactic extinction and inclination effects.

^b Radius of a galaxy at the isophotal level 25 mag/arcsec² in the B band corrected for Galactic extinction and inclination effects.

^c References: 1 – Bruevich et al. (2007), 2 – Gusev & Efremov (2013), 3 – Gusev (2006a,b), 4 – Gusev & Park (2003), 5 – Artamonov et al. (1999), 6 – Gusev et al. (2015), 7 – Artamonov, Bruevich & Gusev (1997).

gions are star complexes with diameters of several hundred parsecs (Elmegreen & Efremov 1996; Efremov & Elmegreen 1998). The sizes of the largest complexes can reach 2 kpc (Elmegreen et al. 1996). Common star complexes are huge groups of relatively young stars, associations, and clusters. Younger clusters form within the larger and older ones. Complexes are the largest and oldest ‘clusters’, the final step in the hierarchical sequence of embedded young star groups. Their sizes are limited by the effective thickness of the galactic gaseous discs. The flocculent spiral arms and some spurs from the grand design spirals are, plausibly, sheared older complexes. The sizes of the SF regions studied here are within the range from several tens to ~ 1000 pc, with a mean value ~ 300 pc.

Being bright, SF regions can be observed in nearby galaxies as objects of magnitude 16 – 20 with emission spectra, but they cannot be resolved into separate stars. Our linear resolution, ≈ 40 pc in the nearest galaxies NGC 628 and NGC 6946, does not allow us to separate young star clusters and OB associations: smaller star clusters will be observed as star-like objects with sizes ≈ 40 pc. In more distant galaxies, we can observe SF regions with sizes of 200–300 pc, i.e. star complexes are conglomerates of young star clusters and/or associations. Young massive star clusters (YMCs), embedded in SF regions, are dense aggregates of young stars, formed at essentially the same time in the same region of space (Portegies Zwart, McMillan & Gieles 2010). Most of the objects studied here are complexes of young massive clusters. From now on, we will use the common term ‘YMC complex’ for the studied stellar populations in SF regions. It should be realized that this term covers young objects of different types: star complexes, cluster complexes, stellar aggregates, OB associations, and star clusters.

The typical gas velocities in an individual H II region are $15 - 30 \text{ km s}^{-1}$ – the velocity of hydrogen atoms at a temperature of 10^4 K, as well as the velocity of the stellar wind. At such velocities, the lifetime of an H II region with a typical size of about 100 pc is about 3 – 7 Myr. After a few Myrs, when the surrounding gas is blown up, the SF region exists in the form of bounded stellar agglomerates, which are referred to as star clusters by Gieles & Portegies Zwart (2011). Ionised gas is not observed around star clusters older than 10 Myr. Thus, we study in the present paper only star clusters/cluster complexes younger than 10 Myr.

A study of the earliest stages of these clusters and their complexes is a difficult task because of the impact of gas and dust on the observations of young massive clusters. Accounting for the ef-

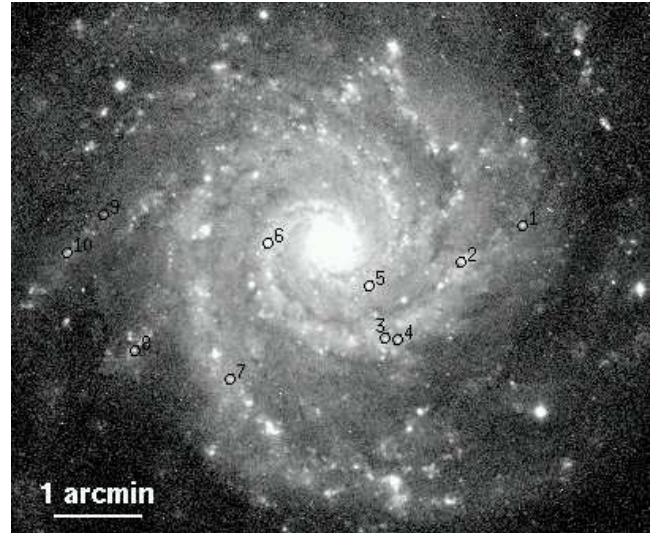


Figure 1. B image of NGC 628 and positions of the galaxy’s star forming regions. The numbers of the star forming regions from Table 3 are indicated. North is upward and East is to the left.

fects of gas and dust on observations of YMCs and their complexes is very important for the interpretation of multicolour photometry in terms of the initial mass function (IMF) and the star formation rate (SFR) history. Despite a huge amount of both spectroscopic and photometric observations of the extragalactic giant H II regions, SF regions, the overlaps of the spectroscopic observations of SF regions with the photometric ones are very poor. Using both techniques, we can eliminate the degeneracy between age and extinction, and between age and metallicity. These degeneracies present a hurdle to the analysis of photometric data (Scalo 1986). In addition, continuum and line emissions from ionised gas rival the stellar luminosity at optical wavelengths (see compilations in Reines et al. 2010).

In the case of massive star forming regions, the nebula emission is strong enough to affect the integrated broadband photometry. Reines et al. (2010) found that nebular line emission is significant in many commonly used broad-band *Hubble Space Telescope* (HST) filters, including the F555W V band and the F435W B band. Emission lines detected via spectroscopy can be used for

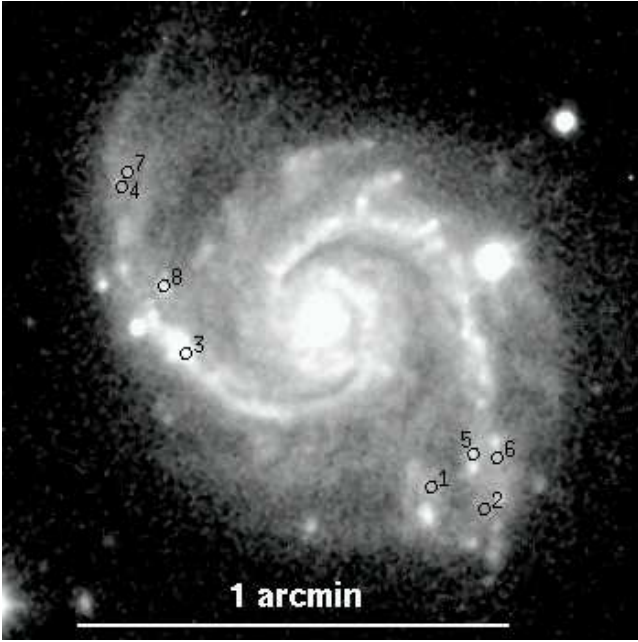


Figure 2. Same as Fig. 1, but for NGC 783.

disentangling the effects of extinction, accounting for the impact of the nebula emission on integrated broadband photometry, and serve as valuable diagnostics of gas abundances (see [Dinerstein 1990](#); [Sakhibov & Smirnov 1990](#); [Reines et al. 2010](#), and references therein). In other words, the combination of spectroscopic and multicolour photometric observations of SF regions provides the true colours and metallicities of young massive cluster complexes. This is necessary to account for the nebular emission impact and to eliminate ‘age–extinction’ and ‘age–metallicity’ degenerations in the comparative analysis with the theoretical evolutionary models of star clusters. Hereafter, we call the colours and luminosities, which are corrected for both the extinction and the nebula emission in broad bands, the ‘true’ colours and luminosities.

With these ideas in mind, several years ago we started simultaneous spectroscopic and photometric observations of SF regions in nearby galaxies. We should outline the progress in the solution of the above mentioned problem of degeneracies achieved by coupling the spectroscopy with *UBVI* photometry of star clusters in M82 ([Konstantopoulos et al. 2009](#)). Having combined information from spectroscopy and imaging, [Konstantopoulos et al. \(2009\)](#) found the disc clusters to form a uniform population, displaying no positional dependencies with respect to age. Unlike current research, [Konstantopoulos et al. \(2009\)](#) studied relatively older objects using absorption spectra. The spectroscopic data itself plays an important role in the study of the chemical evolution of galaxies, where oxygen and nitrogen are key elements. These aspects of the application of our spectral observations results, as well as the data reduction, are summarised in our previous papers ([Gusev et al. 2012](#); [Gusev et al. 2013](#)).

This paper is organized as follows. The observations and reduction are described in Section 2. Section 3 presents the observed photometric parameters of the SF regions. The reduction for the light absorption, and the analysis of the observational effects caused by observation constraints, are described in Section 4. In Section 5 we compare the photometric properties of the cluster complexes in the studied SF regions with the synthetic colours of

evolution models of star clusters. Section 6 describes the estimation of the physical parameters of the studied SF regions. In Section 7 we also present a comparative analysis of the derived true colours of the YMC complexes with the intrinsic colours of 650 Galactic open clusters derived by [Kharchenko et al. \(2005a\)](#) and [Kharchenko et al. \(2005b\)](#) and the synthetic colours of the evolution models. We discuss our results in Section 8. Some conclusions are presented in Section 9.

2 OBSERVATIONS AND DATA REDUCTION

The galaxy sample is presented in Table 1, where fundamental parameters from the LEDA¹ database ([Paturel et al. 2003](#)) are provided. The morphological type of the galaxy is given in column (2), the apparent and absolute magnitudes are listed in columns (3) and (4), the inclination and position angles are listed in columns (5) and (6), and the isophotal radius in arcmin and kpc are listed in columns (7) and (8). The adopted distances are given in column (9). Finally, the Galactic absorption and the dust absorption due to the inclination of a galaxy are presented in columns (10) and (11). The Galactic absorptions, $A(B)_{\text{Gal}}$, are taken from the NED² database. The other parameters are taken from the LEDA database ([Paturel et al. 2003](#)). Maps of the galaxies are given in Figs. 1–7. The adopted value of the Hubble constant is equal to $H_0 = 75 \text{ km s}^{-1} \text{ Mpc}^{-1}$.

The photometric (*UBVRI*) and spectrophotometric ($H\alpha$ line) results for the galaxies from our sample were published earlier (see the notes in Table 1), with the exception of the $H\alpha$ spectrophotometric observations for NGC 6946 and NGC 7331. In Section 2.1 we give a brief compilation of our earlier published results.

2.1 Observations

UBVRI CCD observations of NGC 628, NGC 783, NGC 6217, NGC 6946, NGC 7331, and NGC 7678 were obtained in 2002–2006 with the 1.5 m telescope of the Maidanak Observatory (Institute of Astronomy of the Academy of Sciences of Uzbekistan) using a SITe-2000 CCD array. The focal length of the telescope is 12 m. For a detailed description of the telescope and the CCD camera, see [Artamonov et al. \(2010\)](#). With broadband *U*, *B*, *V*, *R*, and *I* filters, the CCD array realizes a photometric system close to the standard Johnson–Cousins *UBVRI* system. The camera is cooled with liquid nitrogen. The size of the array is 2000×800 pixels. It provides a $8.9 \times 3.6 \text{ arcmin}^2$ field of view with an image scale of $0.267 \text{ arcsec pixel}^{-1}$. The seeing during our observation sessions was about $0.7 - 1.1 \text{ arcsec}$.

Since the angular sizes of NGC 6946 and NGC 7331 are larger than the field of view, we acquired two separate images for the northern and southern parts of NGC 6946 and one image for the central part of NGC 7331.

The *UBVRI* observations of NGC 2336 were carried out in 2001 with the 1.8 m telescope of the Bohyunsan Optical Astronomy Observatory (Korea Astronomy and Space Science Institute) equipped with a CCD camera at the Ritchey–Chrétien f/8 focus. The camera was a SITe AR-coated 2048×2048 pixel array, with a plate scale of $0.34 \text{ arcsec pixel}^{-1}$. The field of view was about

¹ <http://leda.univ-lyon1.fr/>

² <http://ned.ipac.caltech.edu/>



Figure 3. Same as Fig. 1, but for NGC 2336.

11.7×11.7 arcmin². The seeing was 1.7–2.3 arcsec (Gusev & Park 2003).

Spectrophotometric H α observations of three galaxies from our sample (NGC 628, NGC 6946, and NGC 7731) were made on 26 September 2006 with the 1.5-m telescope of the Mt. Maidanak Observatory with the SI-4000 CCD camera. The chip size, 4096×4096 pixels, provides a field of view of 18.1×18.1 arcmin², with an image scale of 0.267 arcsec pixel⁻¹. The total exposure time was 1200 s (4×300 s) for NGC 628 and 900 s (3×300 s) for NGC 6946 and NGC 7731. The seeing was 0.9 – 1.2 arcsec.

A wide-band interference H α filter ($\lambda_{eff} = 6569\text{\AA}$, FWHM = 44\AA) was used for the observations. The filter parameters provide H α + [N II] $\lambda\lambda 6548 + \lambda\lambda 6584$ imaging for the nearby galaxies NGC 628, NGC 6946, and NGC 7731.

2.2 Data reduction

The reduction of the photometric and spectrophotometric data was carried out using standard techniques, with the European Southern Observatory Munich Image Data Analysis System³ (ESO-MIDAS). The main image reduction stages were as follows:

- (a) Correction for bias and flat field;
- (b) Removal of cosmic ray traces;
- (c) Determining the sky background, then subtracting it from each

³ <http://www.eso.org/sci/software/esomidas/>

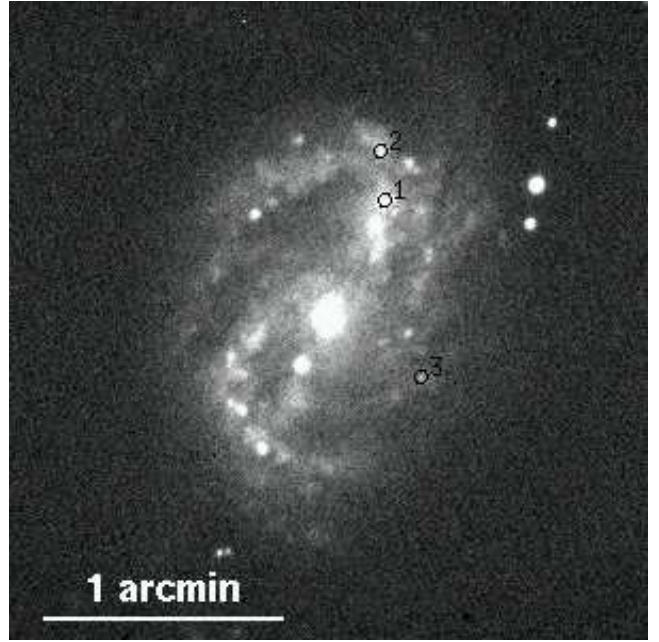


Figure 4. Same as Fig. 1, but for NGC 6217.

image frame;

(d) Aligning the images;

(e) Normalizing and joining the northern and southern parts of the galaxy (for NGC 628 and NGC 6946 in the *U*, *B*, *V*, *R*, and *I* pass-bands);

(f) Adding up the galaxy images taken with the same filter;

(g) Absolute calibration.

The absolute calibration of the photometric data involved reducing the data from the instrumental photometric system to the standard Johnson–Cousins system and correcting for the air mass using the derived colour equations and the results of the aperture photometry of the galaxy.

We derived the colour equations and corrected for atmospheric extinction using observations of stars from the fields of Landolt (1992) PG 0231+051, PG 2213–006, PG 2331+055, SA 92, SA 110, SA 111, SA 113, and SA 114, acquired on the same nights in the *U*, *B*, *V*, *R*, *I*, and H α filters in the wide air mass interval. A detailed study of the instrumental photometric system and the atmospheric extinction at the Maidanak Observatory was presented in Artamonov et al. (2010).

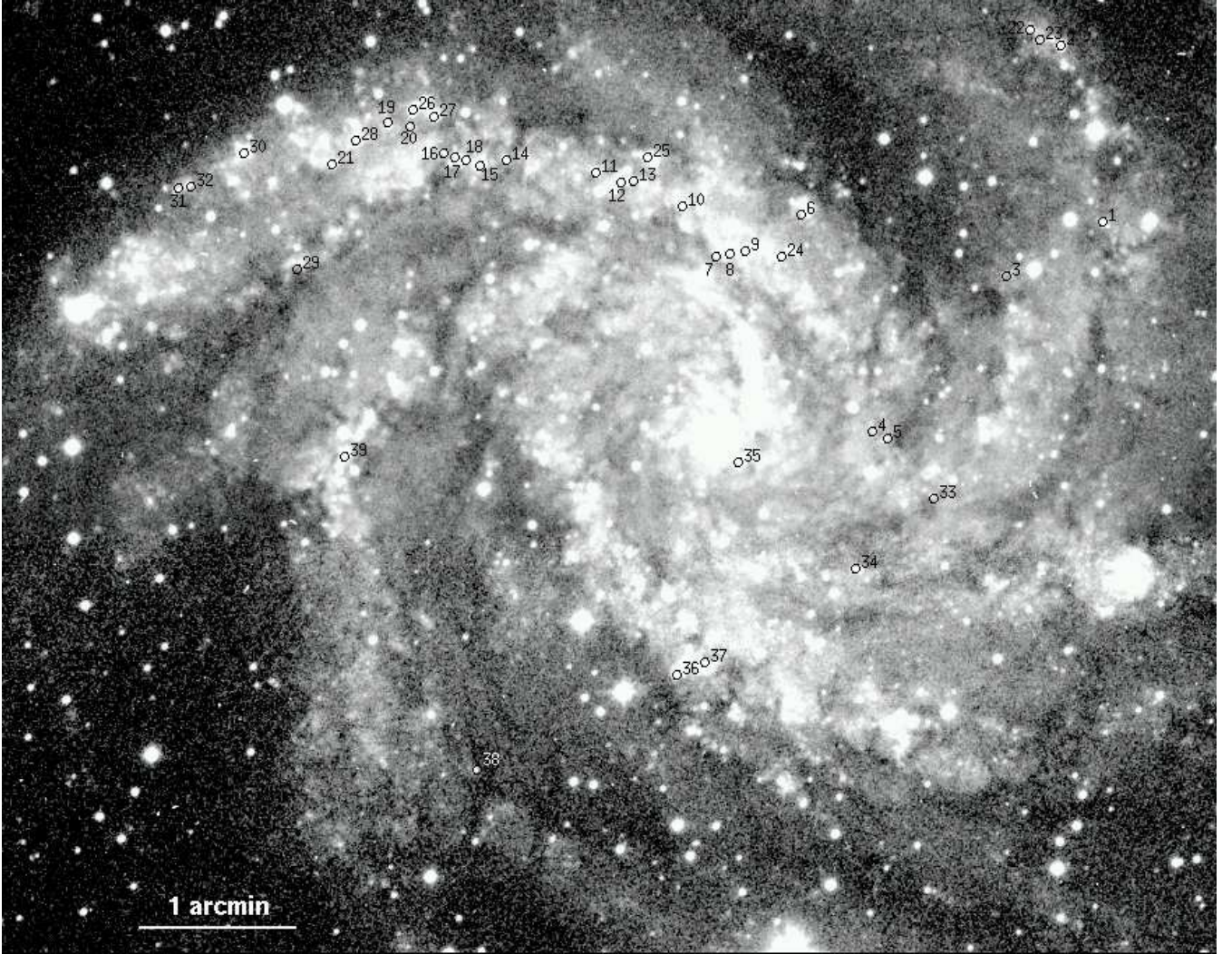
In addition, the aperture photometric data for the galaxies from the LEDA database (Paturel et al. 2003) are used for the absolute calibration of the galaxies. The uncertainties of our photometric data and zero-point error for the galaxies are presented in Table 2.

The spectrophotometric data reduction and the calibration of H α fluxes were described in detail in Gusev & Efremov (2013). The calibration of H α fluxes was made using the results of the spectrophotometric observations of Belley & Roy (1992) and Kennicutt & Hodge (1980) for NGC 628 and NGC 6946. We adopted the value 3.70×10^{-18} erg s⁻¹ cm⁻²/ADU for the coefficient of reduction from our instrumental H α flux to the flux in physical units for all three galaxies. Corrections for the air mass and the radial velocity were also taken into account.

The derived spectrophotometric H α + [N II] fluxes from the

Table 2. The photometric accuracies and image scales of the galaxies.

Galaxy	ΔB (zero-point) (mag)	$\Delta(U - B)$ (mag)	$\Delta(B - V)$ (mag)	$\Delta(V - R)$ (mag)	$\Delta(V - I)$ (mag)	scale (pc/arcsec)
NGC 628	0.03	0.10	0.03	0.02	0.03	34.9
NGC 783	0.15	0.04	0.02	0.03	0.02	342
NGC 2336	0.02	0.03	0.04	0.06	0.07	156
NGC 6217	0.13	0.11	0.02	0.09	0.09	99.9
NGC 6946	0.06	0.06	0.02	0.04	0.04	28.6
NGC 7331	0.02	0.11	0.03	0.03	0.03	68.4
NGC 7678	0.04	0.04	0.02	0.01	0.03	232

**Figure 5.** Same as Fig. 1, but for NGC 6946.

H II regions are presented in Table 3. The data are not corrected for interstellar reddening.

In Fig. 8 we compare our spectrophotometric fluxes (see Table 3) in three galaxies with the spectroscopic H α + [N II] fluxes (Gusev et al. 2012; Gusev et al. 2013). Fig. 8 shows that the spectroscopic flux value is $\sim 40\%$ of the total flux. The spectroscopic flux values are lower limits for the absolute fluxes for slit spectroscopy measurements, because not all radiation from the H II re-

gions falls into the slit. The lack of H II regions with $F_{\text{spec}} > F_{\text{phot}}$ testifies to the correctness of the mutual calibration of the spectral fluxes with the spectrophotometric ones.

The linear scales of our images calculated for the adopted distances to the galaxies are given in the last column of Table 2.

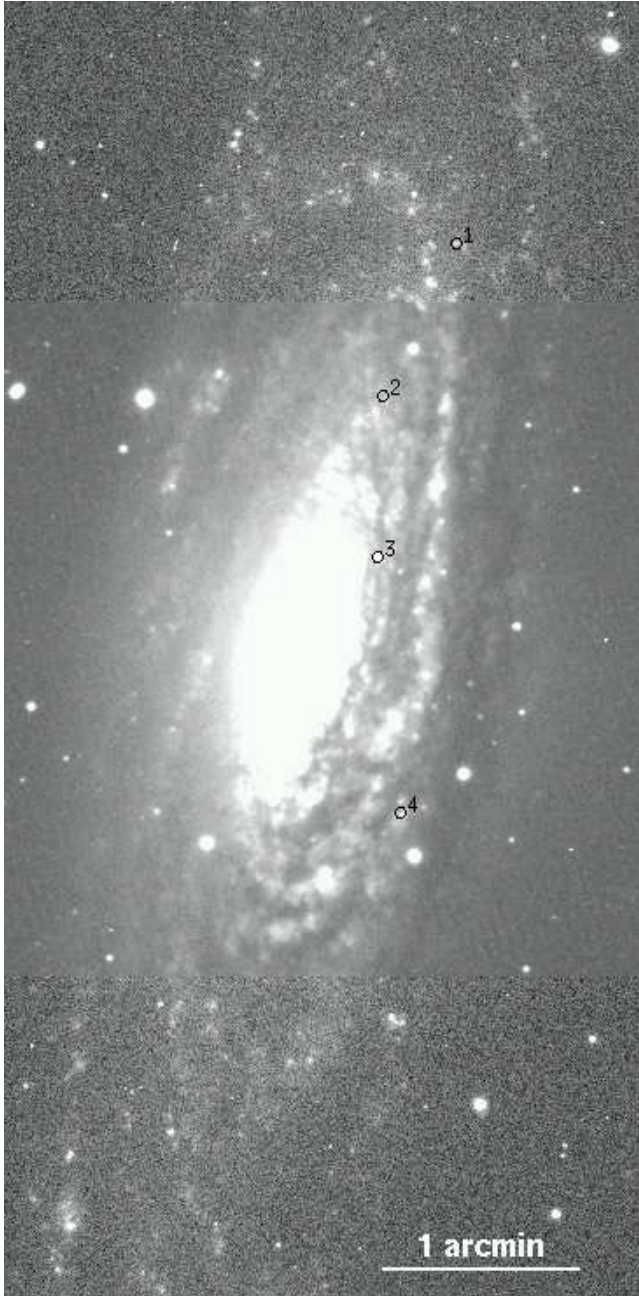


Figure 6. *B* (central part) and $H\alpha$ (northern and southern parts) image of NGC 7331. Numbering of star forming regions and the orientation are as in Fig. 1.

3 PHOTOMETRIC PARAMETERS OF STAR FORMING REGIONS

We identified the SF regions in NGC 628 and NGC 6946 using the list of $H\text{II}$ regions of [Belley & Roy \(1992\)](#). The identification of the SF regions in the other galaxies was made by eye. Maps of the galaxies with identified star forming complexes are presented in Figs. 1–7.

We took the geometric mean of the major and minor axes of the star forming complex for the SF region's characteristic diameter d : $d = \sqrt{d_{\max} \times d_{\min}}$. We measured d_{\max} and d_{\min} from the radial V profiles at the half-maximum brightness level (FWHM) for regions having a starlike profile, or by the distance between the points of

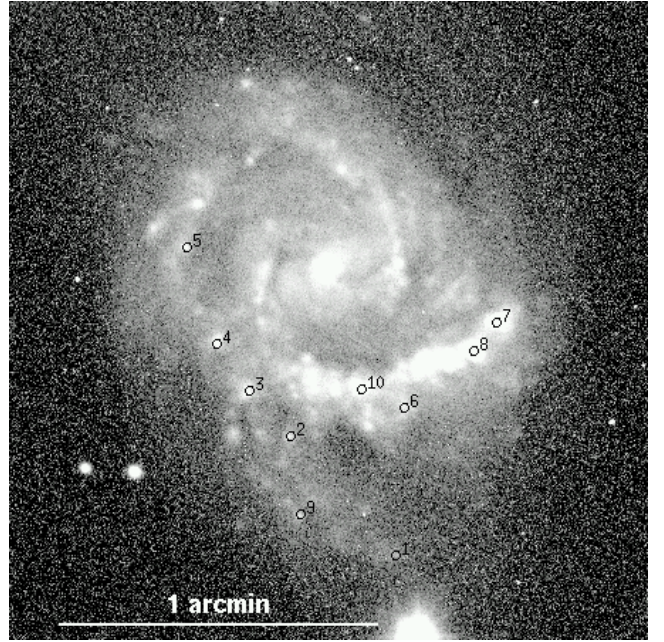


Figure 7. Same as Fig. 1, but for NGC 7678.

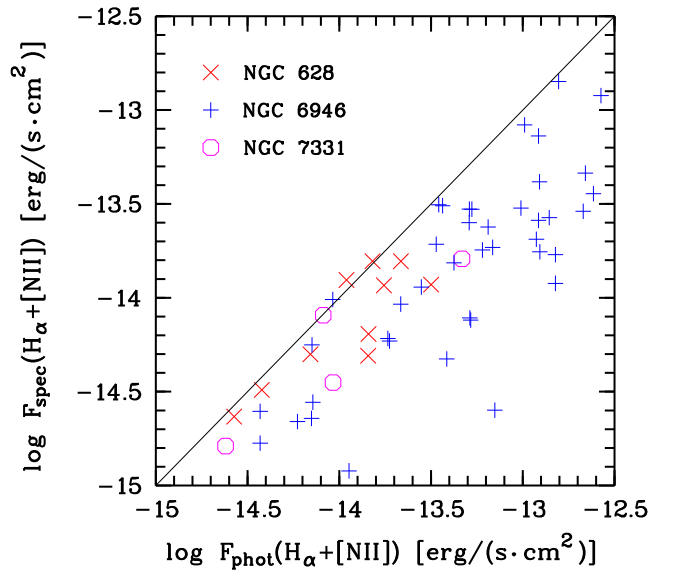


Figure 8. Comparison between the spectroscopic (spec) and spectrophotometric (phot) $H\alpha$ + $[N\text{II}]$ fluxes for $H\text{II}$ regions based on our data.

maximum flux gradient for regions having extended (diffuse) profiles. We adopted the seeing as the error of the size measurements, which definitely exceeds all other errors.

The measurements of the apparent total B magnitude and colour indices $U - B$, $B - V$, $V - R$, and $V - I$ were made within a round aperture. To measure B magnitudes, we used an aperture size equal to the sum of the d_{\max} and the seeing in the B band; in the case of measurements of colour indices, the aperture size is equal to d_{\max} .

The galactic background was subtracted from the flux, measured inside the round aperture. For the galactic background, we

Table 3. Photometric parameters of the star forming regions.

H II region	Ref. ^a	N-S ^b (arcsec)	E-W ^b (arcsec)	<i>B</i> (mag)	<i>M_B</i> (mag)	<i>U</i> − <i>B</i> (mag)	<i>B</i> − <i>V</i> (mag)	<i>V</i> − <i>R</i> (mag)	<i>V</i> − <i>I</i> (mag)	log <i>F</i> (H α) ([erg s ^{−1} cm ^{−2}])
1	2	3	4	5	6	7	8	9	10	11
NGC 628										
1	94	+12.5	+129.0	19.91	−9.38 ± 0.01	−0.70 ± 0.01	0.11 ± 0.01	0.23 ± 0.01	0.51 ± 0.01	−14.16 ± 0.01
2	92	−12.0	+87.7	19.16	−10.13 ± 0.01	−0.33 ± 0.02	0.24 ± 0.01	0.36 ± 0.01	0.76 ± 0.01	−13.84 ± 0.01
3	77	−64.3	+36.5	20.54	−8.75 ± 0.02	−0.78 ± 0.02	0.17 ± 0.04	0.87 ± 0.04	0.52 ± 0.06	−13.96 ± 0.01
4	75	−65.4	+45.0	20.15	−9.14 ± 0.03	−0.49 ± 0.03	0.10 ± 0.03	0.24 ± 0.04	0.04 ± 0.06	−14.57 ± 0.01
5	73	−28.8	+25.3	19.55	−9.74 ± 0.01	−0.69 ± 0.02	0.04 ± 0.03	0.41 ± 0.04	0.60 ± 0.05	−13.84 ± 0.01
6	25	+0.2	−43.0	19.44	−9.85 ± 0.01	−0.62 ± 0.02	0.08 ± 0.03	0.09 ± 0.04	0.32 ± 0.06	−14.42 ± 0.01
7	62	−91.8	−68.1	20.11	−9.18 ± 0.02	−0.72 ± 0.02	0.18 ± 0.02	0.76 ± 0.02	0.55 ± 0.03	−13.76 ± 0.01
8	58	−72.0	−132.6	19.76	−9.53 ± 0.01	−0.89 ± 0.01	0.11 ± 0.01	0.64 ± 0.01	0.33 ± 0.02	−13.66 ± 0.01
9	35	+19.7	−153.1	21.50	−7.79 ± 0.02	−0.99 ± 0.02	0.27 ± 0.02	0.70 ± 0.02	−0.16 ± 0.06	−13.82 ± 0.01
10	38	−6.4	−177.9	18.82	−10.47 ± 0.01	−0.51 ± 0.01	0.15 ± 0.01	0.38 ± 0.01	0.55 ± 0.01	−13.50 ± 0.01
NGC 783										
1	—	−24.3	+16.0	22.23	−12.01 ± 0.12	−0.30 ± 0.16	0.20 ± 0.18	0.54 ± 0.16	0.74 ± 0.20	—
2	—	−27.5	+23.7	20.85	−13.39 ± 0.02	0.19 ± 0.04	0.54 ± 0.03	0.19 ± 0.05	0.80 ± 0.05	—
3	—	−4.8	−19.7	20.67	−13.57 ± 0.02	−0.24 ± 0.02	0.31 ± 0.04	0.30 ± 0.06	0.61 ± 0.08	—
4	—	+19.5	−29.1	21.71	−12.53 ± 0.04	−0.15 ± 0.05	0.54 ± 0.07	0.44 ± 0.07	1.07 ± 0.07	—
5	—	−19.5	+22.1	21.81	−12.43 ± 0.02	−0.37 ± 0.03	0.37 ± 0.03	0.20 ± 0.05	0.45 ± 0.06	—
6	—	−20.0	+25.6	22.12	−12.12 ± 0.05	−0.52 ± 0.05	0.53 ± 0.07	0.40 ± 0.08	0.81 ± 0.10	—
7	—	+21.6	−28.3	21.83	−12.41 ± 0.04	−0.25 ± 0.05	0.44 ± 0.07	0.41 ± 0.07	0.53 ± 0.11	—
8	—	+5.1	−22.9	20.92	−13.32 ± 0.04	−0.62 ± 0.04	0.28 ± 0.07	0.17 ± 0.10	0.10 ± 0.15	—
NGC 2336										
1	—	−113.8	+33.5	19.83	−12.71 ± 0.03	−0.69 ± 0.05	0.42 ± 0.03	0.34 ± 0.04	0.51 ± 0.04	—
2	28	−89.0	−40.0	19.84	−12.70 ± 0.03	−0.30 ± 0.05	0.39 ± 0.03	0.52 ± 0.02	0.50 ± 0.03	—
3	27a	−71.8	+0.2	20.19	−12.35 ± 0.05	−0.43 ± 0.06	0.27 ± 0.07	0.44 ± 0.08	0.69 ± 0.08	—
4	26	−47.8	−10.5	19.51	−13.03 ± 0.05	−0.58 ± 0.07	0.52 ± 0.06	0.54 ± 0.07	0.95 ± 0.08	—
5	22	−27.5	−9.8	20.55	−11.99 ± 0.03	−0.51 ± 0.07	0.54 ± 0.05	0.54 ± 0.05	0.94 ± 0.07	—
6	17	+17.5	+85.4	19.80	−12.74 ± 0.01	−0.50 ± 0.03	0.32 ± 0.02	0.45 ± 0.02	0.52 ± 0.03	—
7	5	+95.9	+13.6	21.07	−11.47 ± 0.03	−0.53 ± 0.08	0.44 ± 0.04	0.73 ± 0.04	0.76 ± 0.05	—
8	27d	−82.5	−9.5	19.67	−12.87 ± 0.01	−0.42 ± 0.03	0.42 ± 0.02	0.41 ± 0.03	0.59 ± 0.04	—
9	—	−62.6	+8.1	20.66	−11.88 ± 0.03	−0.36 ± 0.07	0.48 ± 0.04	0.48 ± 0.06	0.48 ± 0.07	—
10	19	+3.4	+43.8	19.42	−13.12 ± 0.02	−0.46 ± 0.03	0.27 ± 0.02	0.36 ± 0.03	0.53 ± 0.04	—
11	16	+18.2	+38.7	20.90	−11.64 ± 0.05	−0.70 ± 0.09	0.52 ± 0.06	0.48 ± 0.05	0.83 ± 0.07	—
12	10	+52.3	+0.2	20.38	−12.16 ± 0.05	−0.25 ± 0.10	0.55 ± 0.06	0.52 ± 0.06	0.82 ± 0.08	—
13	8	+68.1	−34.5	19.33	−13.21 ± 0.03	−0.66 ± 0.04	0.48 ± 0.03	0.51 ± 0.03	0.71 ± 0.03	—
14	2	+142.0	−11.5	20.01	−12.53 ± 0.03	−0.65 ± 0.04	0.32 ± 0.03	0.37 ± 0.04	0.44 ± 0.05	—
15	30	−109.0	−32.1	19.93	−12.61 ± 0.03	−0.58 ± 0.05	0.39 ± 0.03	0.32 ± 0.03	0.47 ± 0.04	—
16	27b	−77.3	−3.6	20.52	−12.02 ± 0.08	−0.26 ± 0.13	0.40 ± 0.12	0.43 ± 0.13	0.61 ± 0.13	—
17	21	−26.1	+48.3	18.26	−14.28 ± 0.01	−0.33 ± 0.01	0.29 ± 0.01	0.43 ± 0.01	0.56 ± 0.02	—
18	29	−94.5	−37.3	21.20	−11.34 ± 0.04	−0.50 ± 0.10	0.38 ± 0.06	0.66 ± 0.07	0.57 ± 0.09	—
19	27e	−83.9	−4.3	21.12	−11.42 ± 0.10	−0.19 ± 0.15	0.39 ± 0.13	0.37 ± 0.15	0.49 ± 0.17	—
20	—	−31.6	+48.6	21.14	−11.40 ± 0.03	−0.45 ± 0.05	0.71 ± 0.04	0.34 ± 0.05	0.70 ± 0.06	—
21	—	−19.3	+47.6	20.87	−11.67 ± 0.05	−0.24 ± 0.10	0.59 ± 0.09	0.39 ± 0.12	0.43 ± 0.17	—
22	—	+27.2	−62.7	21.76	−10.78 ± 0.02	−0.91 ± 0.04	0.68 ± 0.03	0.61 ± 0.03	0.65 ± 0.04	—
23	23	+24.4	−61.7	20.27	−12.27 ± 0.01	−0.97 ± 0.02	0.57 ± 0.02	0.52 ± 0.02	0.68 ± 0.03	—
24	9	+62.6	+48.3	20.84	−11.70 ± 0.05	−0.57 ± 0.09	0.45 ± 0.05	0.25 ± 0.05	0.46 ± 0.06	—
25	—	+67.7	+44.5	20.27	−12.27 ± 0.03	−0.60 ± 0.05	0.55 ± 0.04	0.22 ± 0.04	0.38 ± 0.06	—
26	—	+77.7	−5.3	21.18	−11.36 ± 0.04	−0.64 ± 0.06	0.57 ± 0.06	0.35 ± 0.07	0.55 ± 0.07	—
27	7	+80.8	−4.6	20.07	−12.47 ± 0.02	−0.31 ± 0.05	0.32 ± 0.05	0.25 ± 0.06	0.63 ± 0.07	—
28	4	+111.7	−31.1	20.73	−11.81 ± 0.04	−0.60 ± 0.09	0.49 ± 0.06	0.56 ± 0.06	0.42 ± 0.07	—
NGC 6217										
1	—	+29.8	+13.9	17.19	−14.35 ± 0.01	−0.09 ± 0.01	0.58 ± 0.01	0.50 ± 0.01	1.13 ± 0.01	—
2	—	+42.2	+13.0	17.66	−13.44 ± 0.04	−0.56 ± 0.05	0.17 ± 0.07	0.45 ± 0.09	0.99 ± 0.10	—
3	—	−14.6	+23.2	19.83	−11.67 ± 0.08	−0.83 ± 0.05	0.06 ± 0.06	0.53 ± 0.07	0.65 ± 0.16	—
NGC 6946										
1	116	+79.7	+146.5	20.09	−8.76 ± 0.01	−0.33 ± 0.01	0.41 ± 0.02	0.64 ± 0.02	0.61 ± 0.03	−13.73 ± 0.01
2	143	+146.9	+130.5	18.76	−10.09 ± 0.01	−0.37 ± 0.01	0.50 ± 0.01	0.85 ± 0.01	0.79 ± 0.02	−12.80 ± 0.01
3	—	+58.9	+110.0	20.57	−8.28 ± 0.07	−0.64 ± 0.05	0.53 ± 0.07	0.23 ± 0.07	0.67 ± 0.11	−13.99 ± 0.01
4	—	−0.3	+58.8	21.52	−7.33 ± 0.08	−0.45 ± 0.08	0.62 ± 0.12	0.60 ± 0.13	1.05 ± 0.17	−14.14 ± 0.01
5	—	−2.7	+64.6	20.73	−8.12 ± 0.06	−0.02 ± 0.10	0.55 ± 0.15	0.36 ± 0.18	0.93 ± 0.21	−14.43 ± 0.02

^a ID number of H II region by [Belley & Roy \(1992\)](#) for NGC 628 and NGC 6946, and by [Gusev & Park \(2003\)](#) for NGC 2336.^b Galactocentric coordinates. Positive values correspond to the northern and western positions.

Table 3. Continued

H II region	Ref. ^a	N-S ^b (arcsec)	E-W ^b (arcsec)	<i>B</i> (mag)	<i>M_B</i> (mag)	<i>U</i> - <i>B</i> (mag)	<i>B</i> - <i>V</i> (mag)	<i>V</i> - <i>R</i> (mag)	<i>V</i> - <i>I</i> (mag)	log <i>F</i> (H α) ([erg s ⁻¹ cm ⁻²])
1	2	3	4	5	6	7	8	9	10	11
NGC 6946										
6	149	+82.6	+31.6	18.11	-10.74 ± 0.01	-0.41 ± 0.01	0.40 ± 0.01	0.32 ± 0.01	0.69 ± 0.01	-13.22 ± 0.01
7	—	+66.3	-1.2	21.29	-7.56 ± 0.07	-0.50 ± 0.08	0.32 ± 0.14	0.67 ± 0.18	0.44 ± 0.41	-13.95 ± 0.01
8	—	+67.7	+4.1	19.36	-9.49 ± 0.02	-0.08 ± 0.02	0.51 ± 0.03	0.39 ± 0.05	0.91 ± 0.06	-14.15 ± 0.01
9	150	+68.5	+10.2	18.39	-10.46 ± 0.01	-0.36 ± 0.01	0.47 ± 0.02	0.65 ± 0.02	0.89 ± 0.03	-12.91 ± 0.01
10	10	+85.5	-14.0	18.58	-10.27 ± 0.02	-0.32 ± 0.02	0.54 ± 0.02	0.44 ± 0.02	0.69 ± 0.02	-13.19 ± 0.01
11	—	+98.6	-46.8	18.92	-9.93 ± 0.01	-0.31 ± 0.01	0.57 ± 0.02	0.72 ± 0.02	0.79 ± 0.05	-13.01 ± 0.01
12	8	+94.9	-37.5	18.28	-10.57 ± 0.01	-0.31 ± 0.01	0.47 ± 0.01	0.43 ± 0.01	0.79 ± 0.02	-13.16 ± 0.01
13	6	+95.4	-32.4	19.82	-9.03 ± 0.02	-0.33 ± 0.03	0.69 ± 0.04	0.73 ± 0.04	1.22 ± 0.05	-13.47 ± 0.01
14	24	+103.4	-81.0	20.12	-8.73 ± 0.02	-0.22 ± 0.03	0.66 ± 0.03	0.78 ± 0.02	0.77 ± 0.04	-13.44 ± 0.01
15	25	+101.0	-91.4	18.46	-10.39 ± 0.01	-0.43 ± 0.01	0.40 ± 0.01	0.65 ± 0.02	0.73 ± 0.02	-12.82 ± 0.01
16	29	+106.1	-105.0	20.32	-8.53 ± 0.01	-0.30 ± 0.02	0.70 ± 0.02	1.16 ± 0.02	1.53 ± 0.03	-13.29 ± 0.01
17	28	+104.2	-101.0	18.21	-10.64 ± 0.01	-0.21 ± 0.01	0.61 ± 0.01	0.87 ± 0.01	1.23 ± 0.01	-12.67 ± 0.01
18	26	+103.1	-96.7	19.52	-9.33 ± 0.01	-0.33 ± 0.01	0.49 ± 0.01	0.52 ± 0.01	0.58 ± 0.02	-13.37 ± 0.01
19	16	+117.8	-126.3	19.66	-9.19 ± 0.02	-0.47 ± 0.03	0.44 ± 0.04	0.69 ± 0.03	1.09 ± 0.04	-13.29 ± 0.01
20	—	+116.2	-118.0	21.33	-7.52 ± 0.05	-0.37 ± 0.07	0.25 ± 0.09	0.57 ± 0.11	—	-14.04 ± 0.01
21	19	+101.8	-147.6	18.61	-10.24 ± 0.01	-0.46 ± 0.01	0.35 ± 0.01	0.74 ± 0.01	0.94 ± 0.02	-12.91 ± 0.01
22	146	+153.0	+118.8	19.61	-9.24 ± 0.01	-0.19 ± 0.02	0.54 ± 0.01	0.77 ± 0.01	1.10 ± 0.02	-13.28 ± 0.01
23	145	+149.3	+122.5	19.28	-9.57 ± 0.01	-0.35 ± 0.01	0.53 ± 0.01	0.97 ± 0.01	1.13 ± 0.02	-12.93 ± 0.01
24	151	+66.3	+23.8	19.74	-9.11 ± 0.03	0.33 ± 0.04	0.98 ± 0.04	0.50 ± 0.04	1.05 ± 0.04	-14.15 ± 0.01
25	5	+104.5	-27.1	17.96	-10.89 ± 0.01	-0.51 ± 0.02	0.38 ± 0.02	0.63 ± 0.03	0.63 ± 0.04	-12.61 ± 0.01
26	15	+122.3	-116.7	18.23	-10.62 ± 0.01	-0.41 ± 0.01	0.36 ± 0.02	0.55 ± 0.02	0.43 ± 0.04	-12.91 ± 0.01
27	14	+119.9	-108.7	17.75	-11.10 ± 0.01	-0.40 ± 0.01	0.35 ± 0.01	0.42 ± 0.02	0.40 ± 0.03	-12.66 ± 0.01
28	17	+110.6	-138.6	18.52	-10.33 ± 0.01	-0.17 ± 0.01	0.46 ± 0.01	0.34 ± 0.01	0.88 ± 0.01	-13.41 ± 0.01
29	—	+61.8	-161.2	18.96	-9.89 ± 0.01	-0.24 ± 0.02	0.50 ± 0.02	0.40 ± 0.02	0.89 ± 0.03	-13.29 ± 0.01
30	39	+105.8	-181.2	17.93	-10.92 ± 0.01	-0.44 ± 0.01	0.59 ± 0.02	0.62 ± 0.01	0.74 ± 0.02	-12.57 ± 0.01
31	—	+92.5	-206.3	19.73	-9.12 ± 0.02	-0.42 ± 0.02	0.31 ± 0.03	0.33 ± 0.04	0.71 ± 0.05	-13.73 ± 0.01
32	—	+93.3	-201.5	19.66	-9.19 ± 0.01	-0.40 ± 0.02	0.46 ± 0.02	0.31 ± 0.02	0.52 ± 0.03	-13.66 ± 0.01
33	—	-25.7	+82.0	21.30	-7.55 ± 0.15	0.03 ± 0.21	0.75 ± 0.20	—	1.53 ± 0.14	-13.28 ± 0.01
34	—	-52.6	+52.4	19.34	-9.51 ± 0.01	-0.38 ± 0.02	0.46 ± 0.03	0.49 ± 0.03	0.75 ± 0.05	-13.46 ± 0.01
35	163	-12.1	+7.6	19.00	-9.85 ± 0.01	0.43 ± 0.02	1.12 ± 0.02	0.53 ± 0.02	1.43 ± 0.02	-13.55 ± 0.01
36	78	-92.9	-15.9	18.58	-10.27 ± 0.02	-0.43 ± 0.03	0.42 ± 0.04	0.71 ± 0.04	0.91 ± 0.06	-12.86 ± 0.01
37	—	-88.1	-5.5	18.21	-10.64 ± 0.02	-0.31 ± 0.02	0.51 ± 0.03	0.33 ± 0.04	0.93 ± 0.04	-13.15 ± 0.01
38	—	-129.1	-92.4	20.41	-8.44 ± 0.01	0.28 ± 0.03	1.03 ± 0.01	0.34 ± 0.01	1.02 ± 0.01	-14.23 ± 0.01
39	49	-9.7	-142.8	18.81	-10.04 ± 0.01	-0.44 ± 0.01	0.39 ± 0.01	0.65 ± 0.01	0.72 ± 0.02	-12.99 ± 0.01
NGC 7331										
1	—	+123.2	+40.4	—	—	—	—	—	—	-14.62 ± 0.01
2	—	+76.8	+18.0	19.66	-11.09 ± 0.04	-0.06 ± 0.05	0.81 ± 0.05	0.68 ± 0.03	1.56 ± 0.03	-14.03 ± 0.01
3	—	+27.4	+16.2	20.05	-10.70 ± 0.04	-0.09 ± 0.06	0.76 ± 0.07	0.49 ± 0.10	1.26 ± 0.12	-14.09 ± 0.02
4	—	-50.2	+23.1	18.34	-12.41 ± 0.02	-0.75 ± 0.02	0.22 ± 0.02	0.41 ± 0.02	0.81 ± 0.03	-13.33 ± 0.01
NGC 7678										
1	—	-54.2	+12.6	21.50	-11.90 ± 0.05	-0.57 ± 0.07	0.55 ± 0.10	0.47 ± 0.10	0.20 ± 0.21	—
2	—	-31.8	-7.1	20.73	-12.67 ± 0.03	-0.52 ± 0.05	0.41 ± 0.06	0.19 ± 0.07	0.44 ± 0.10	—
3	—	-23.3	-14.8	19.30	-14.10 ± 0.02	-0.43 ± 0.03	0.33 ± 0.04	0.35 ± 0.04	0.59 ± 0.06	—
4	—	-14.5	-21.0	19.47	-13.93 ± 0.02	-0.71 ± 0.03	0.51 ± 0.04	0.58 ± 0.04	0.56 ± 0.06	—
5	—	+3.7	-26.6	20.18	-13.22 ± 0.03	-0.43 ± 0.05	0.31 ± 0.06	0.16 ± 0.08	0.33 ± 0.09	—
6	—	-26.5	+14.2	19.44	-13.96 ± 0.02	-0.23 ± 0.03	0.43 ± 0.04	0.35 ± 0.05	0.79 ± 0.06	—
7	—	-10.5	+31.6	17.47	-15.93 ± 0.01	-0.35 ± 0.01	0.48 ± 0.01	0.39 ± 0.01	0.93 ± 0.01	—
8	—	-15.8	+27.3	17.14	-16.26 ± 0.01	-0.56 ± 0.01	0.36 ± 0.01	0.41 ± 0.01	0.65 ± 0.02	—
9	—	-46.5	-5.2	20.66	-12.74 ± 0.03	-0.67 ± 0.04	0.34 ± 0.06	0.59 ± 0.07	0.43 ± 0.12	—
10	—	-23.0	+6.2	18.29	-15.11 ± 0.01	-0.38 ± 0.02	0.40 ± 0.02	0.26 ± 0.02	0.52 ± 0.03	—

^a ID number of H II region by Belley & Roy (1992) for NGC 628 and NGC 6946, and by Gusev & Park (2003) for NGC 2336.^b Galactocentric coordinates. Positive values correspond to the northern and western positions.

took the average flux from the area close to the SF region which has no bright objects and has a minimal inner diameter greater than the sum of d_{max} and the seeing in the *B* band.

We derived the magnitudes and colour indices for 101 of the 102 SF regions studied in Gusev et al. (2012) and Gusev et al.

(2013). Region No. 1 in NGC 7331 is out of the image in the *UBVRI* bands (Fig. 6).

The photometric parameters of the star formation regions are presented in Table 3. The columns of the table present the following properties: (1) assigned sequence number by Gusev et al. (2012)

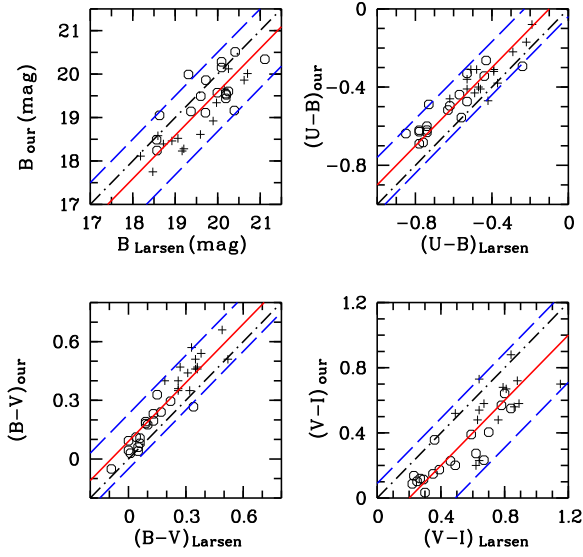


Figure 9. Comparison between our and the reference (Larsen 1999, 2004) B magnitudes (top-left), $U - B$ (top-right), $B - V$ (bottom-left), and $V - I$ (bottom-right) colour indices for star forming regions in NGC 628 and NGC 6946. The pluses are objects in NGC 6946, the circles are objects in NGC 628. The solid lines are linear fits, computed for SF regions (pluses and circles). Dashed lines are upper and lower 95% prediction limits of the linear fit. Dot dashed lines are one-to-one correlation. Magnitudes and colour indices are not corrected for extinction.

and Gusev et al. (2013), (2) cross-reference ID number, (3, 4) apparent coordinates, in arcseconds, relative to the galaxy centre in the plane of the sky, (5) apparent total B magnitude, (6) absolute magnitude M_B , $M_B = B - 5 \log D - 25$, where D is an adopted distance in units of Mpc, (7–10) the colour indices $U - B$, $B - V$, $V - R$, and $V - I$ with their uncertainties, (11) logarithm of spectrophotometric $H\alpha + [N II]$ flux.

The photometric errors in Table 3 correspond to the uncertainties in the aperture photometry. A main source of photometric errors is the uncertainty of the galactic background. Table 3 presents the pure observed data.

Larsen (1999, 2004) studied young star clusters in several nearby galaxies. We can only compare our data with the data of Larsen qualitatively, because of the different apertures, seeings, and photometric systems used. We identified 15 objects in NGC 6946 and 18 objects in NGC 628 from Larsen’s list, which are in common with the objects studied here and in our previous paper Bruevich et al. (2007). In Fig. 9 we compare our $UBVI$ photometry with the results published by Larsen (1999) and Larsen (2004). Fig. 9 shows a good correlation between Larsen’s and our observations,

$$\begin{aligned} B_{\text{our}} &= B_{\text{Larsen}} - (0.41 \pm 0.08) \\ (U - B)_{\text{our}} &= (U - B)_{\text{Larsen}} + (0.10 \pm 0.01) \\ (B - V)_{\text{our}} &= (B - V)_{\text{Larsen}} + (0.09 \pm 0.01) \\ (V - I)_{\text{our}} &= (V - I)_{\text{Larsen}} - (0.20 \pm 0.02) \end{aligned} \quad (1)$$

with the following correlation coefficients for different magnitudes and colour indices: $r_B = 0.98$, $r_{U-B} = 0.92$, $r_{B-V} = 0.94$, and $r_{V-I} = 0.83$.

Our B magnitudes are systematically lower than the B magnitudes measured by Larsen. This is a result of the different apertures used by Larsen (2004) (1.0 arcsec) and by our team (several arcsec-

onds, depending on the size of the SF region). It is notable that the seeing of *HST* images (~ 0.1 arcsec) of Larsen (2004) is ten times better than the seeing of our images (~ 1.0 arcsec). The differences and deviations between our data and the results of Larsen (2004): $B_{\text{our}} = B_{\text{Larsen}} - (0.41 \pm 0.08)$ mag (the standard deviation around the mean is 0.44 mag) and $V_{\text{our}} = V_{\text{Larsen}} - (0.50 \pm 0.07)$ mag (the standard deviation around the mean is 0.45 mag) are in good agreement with the differences and deviations between the space (2004) and the ground (1999) observations of Larsen: $\langle \Delta V_{\text{ground-HST}} \rangle = -0.76 \pm 0.61$ mag for the ground observations with an aperture of 6.4 arcsec and $\langle \Delta V_{\text{ground-HST}} \rangle = -0.29 \pm 0.50$ mag for the ground observations with an aperture of 3.0 arcsec (here 0.61 and 0.50 mag are the standard deviations around the mean). Unfortunately, we can not compare the ground observations of Larsen with ours because of the small number of objects in common.

Fig. 9 and Eq. (1) show that the systematic deviations between the linear fits (solid line) and a one-to-one correlation (dot dashed line), in the cases of $U - B$ and $B - V$, lie within the accuracy limits ≤ 0.1 mag. Note that the deviations for the $B - V$ colour index between the standard Johnson–Cousins and the *HST* photometric systems for young star clusters are ± 0.15 mag by Larsen (2004) and ± 0.17 mag by Holtzman et al. (1995).

In the case of the $V - I$ colour index, there is a negative systematic deviation ≈ 0.20 mag at the lower correlation coefficient. A lower correlation and a quite great systematic deviation 0.20 mag in case of the $V - I$ colours can be caused by a smaller signal-to-noise ratio and a larger background fluctuation in the I passband. In comparison with evolutionary models, we accounted for this systematic deviation using a linear regression, shown in Fig. 9 (bottom-right panel), $V - I = (V - I)_{\text{obs}} + 0.20$.

These $V - I$ colour indices, corrected according to Eq. (1), are given in column (10) of Table 3. Obviously, the $V - I$ data can be used only for qualitative estimations.

4 OBSERVATIONAL EFFECTS

4.1 Light absorption

As mentioned above, combined spectroscopic and multi photometric observations of SF regions provide dereddened colours of the SF regions. The star forming regions studied here constitute a single conglomerate of clouds of interstellar dust, ionised hydrogen, and newly formed star clusters. Much of the light emitted by the stars in the SF region’s clusters undergoes absorption inside rather than outside the region itself. Therefore, if a SF region contains a significant amount of interstellar dust, then the light from the stars of that SF region is strongly attenuated even if the host galaxy is seen face-on.

We assume that the emission from stars embedded in the SF region is absorbed in the same way as the emission in lines of ionised hydrogen surrounding the star clusters in the SF region. In other words, the light extinction for the stars is equal to the light extinction for the emission of ionised gas $A_V(\text{stars}) = A_V(\text{Balmer})$. For a detailed discussion of this topic, see our previous paper (Gusev et al. 2009).

Using this assumption, the measured $UBVRI$ fluxes have been corrected for interstellar reddening using the following expression

$$A_V = \frac{2.5}{k_{H\beta} - k_{H\alpha}} \cdot \log \frac{(I_{H\alpha}/I_{H\beta})_{\text{obs}}}{(I_{H\alpha}/I_{H\beta})_{\text{dereddened}}}.$$

Here, $(I_{H\alpha}/I_{H\beta})_{\text{obs}}$ is the ratio of the intensities I of the Balmer hydrogen emission lines derived from the spectra of the $H II$ regions

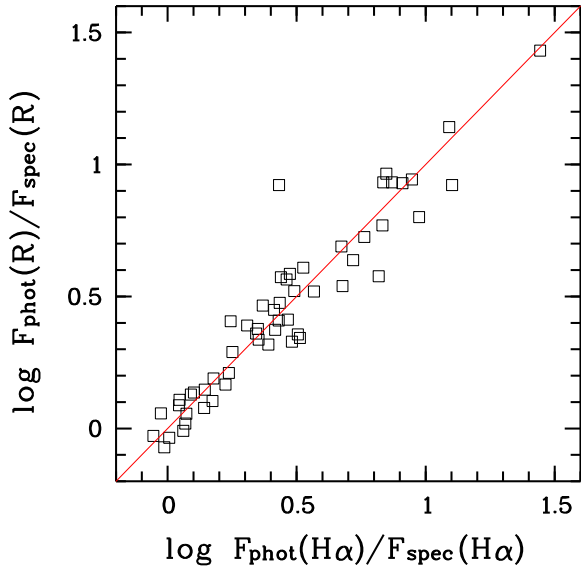


Figure 10. Ratio of fluxes within the round aperture and the area of slit in the R passband versus ratio of fluxes in $H\alpha$ filter. Correlation coefficient is 98%.

of the studied SF regions, while $k_{H\alpha} = A_{H\alpha}/A_V$ and $k_{H\beta} = A_{H\beta}/A_V$ are the absorption coefficients in the emission lines $H\alpha$ and $H\beta$.

We used the theoretical $H\alpha$ to $H\beta$ ratio from [Osterbrock \(1989\)](#), assuming case B recombination and an electron temperature of 10^4 K and the analytical approximation to the Whitford interstellar reddening law by [Izotov, Thuan & Lipovetsky \(1994\)](#). Note that differences between the interstellar extinction laws in different galaxies are negligible for the part of the optical spectra where both lines $H\alpha$ and $H\beta$ belong. The uncertainty of the extinction value is calculated from the measurement errors of the $H\alpha$ and $H\beta$ lines and propagated to the dereddened fluxes. The derived estimates of the extinction A_V are summarised in Table 4.

4.2 Nebular continuum and line emission

A number of authors have discussed the impact of nebular emission on the broadband photometry of young stellar populations (see references therein [Dinerstein 1990](#); [Sakhibov & Smirnov 1990](#); [Reines et al. 2010](#); [Hollyhead et al. 2015](#)). Here we determine the relative contributions of the stellar continuum F_{stars} , nebular continuum $F_{\text{nebula continuum}}$, and emission lines F_{lines} to the total observed flux F_{total} in the broadband filter as follows ([Sakhibov & Smirnov 1990](#)):

$$F_{\text{total}} = F_{\text{stars}} + F_{\text{nebula continuum}} + F_{\text{lines}}. \quad (2)$$

Having obtained the emission line ratios for every SF region in our spectroscopic sample, we derived the characteristic values of the electron temperatures T_e and metallicities Z in the $H\text{II}$ regions in the studied SF regions ([Gusev et al. 2012](#); [Gusev et al. 2013](#)).

One can see in Fig. 8 that the slit in the majority of the cases never transmits the full amount of ionised flux in $H\alpha$. This leads to underestimating the contribution of the nebular emission to the photometric bands. For the three galaxies NGC 628, NGC 6946, and NGC 7331, we used the available spectrophotometric $H\alpha$ fluxes (see Fig. 8 and Table 3) for the absolute calibration of the

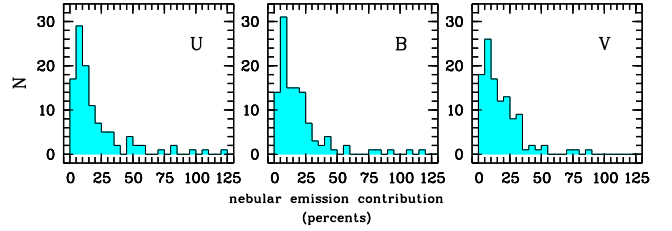


Figure 11. Distributions of studied SF regions over nebular emission contribution in the U band (left), in the B band (centre), and in the V band (right).

emission line intensities derived through spectroscopy. To account for this underestimation for the other four galaxies with unknown $H\alpha$ photometry, we multiplied the absolute fluxes derived through the slit by a factor calculated as the ratio of the flux in the R passband within the round aperture for every $H\text{II}$ region with the flux within the area of the slit: $F_{\text{photometry}}(R)/F_{\text{spectroscopy}}(R)$.

Fig. 10 shows a good correlation (98%) between the used factor $F_{\text{photometry}}(R)/F_{\text{spectroscopy}}(R)$ and the ratio of $H\alpha$ intensities $F_{\text{photometry}}(H\alpha)/F_{\text{spectroscopy}}(H\alpha)$ within the same round aperture and the same area of the slit. The correlation in Fig. 10 was computed using the available spectrophotometric $H\alpha$ fluxes from $H\text{II}$ regions in the three galaxies NGC 628, NGC 6946, and NGC 7331.

This enables us to estimate the relative contributions of the nebular continuum $F_{\text{nebula continuum}}$, using the equations for the continuum emission near the limits of the hydrogen series emission, free-free emission, and two-photon emission, given in [Lang \(1978\)](#), [Kaplan & Pikelner \(1979\)](#), [Brown & Mathews \(1970\)](#), and [Osterbrock \(1989\)](#).

The contribution from the nebular line emission was computed through the summation of the emission line intensities that appear in a given photometric band. The fluxes for the non-measured emission lines were computed from the derived estimations of the emission measures EM , using the equations given in [Kaplan & Pikelner \(1979\)](#) and [Osterbrock \(1989\)](#). A total of 18 main lines of interstellar medium were taken into account.

Fig. 11 shows the distributions of the studied SF regions over the relative contribution of the nebular emission to the U , B , and V fluxes.

The number of objects decreases with an increase of the relative contributions of the nebular emission. Approximately 50% of the objects show relative contributions of less than 15% from the total fluxes. This indicates that 50% of the star clusters are older than 4 Myr, according to the evolution of the ratio of the nebular continuum to the total continuum computed in [Reines et al. \(2010\)](#) as a function of wavelength for a Starburst99 SSP. Another 50% of the objects show relative contributions of more than 15% from the total fluxes and are younger than 4 Myr. Note that these estimates are qualitative. Objects with relative contributions of nebular emission to the $UBVR$ broadbands greater than 1 are excluded from further consideration. Such not sensible cases could be observational effects, caused by overestimated absolute $H\alpha$ fluxes, or a wrong computed correction factor $F_{\text{photometry}}(R)/F_{\text{spectroscopy}}(R)$, or by underestimated absolute fluxes in the photometric bands because of differential extinction in the stellar continuum and nebular emission. The estimated relative contributions of the nebular emission to broadband B , $I_B(\text{gas})/I_B(\text{total})$, are displayed in Table 4.

In Fig. 12 we compare the dereddened colours and luminosities (crosses) of the star forming regions in NGC 2336 with the

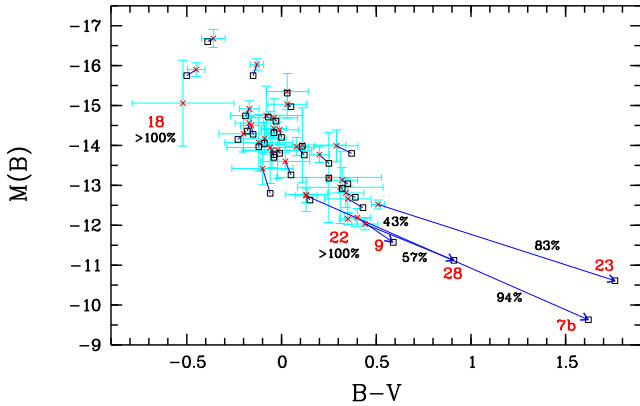


Figure 12. Comparison of the true colours and luminosities of star clusters (open squares) embedded in SF regions with the dereddened ones (crosses) of star forming regions in NGC 2336 in the colour–magnitude diagram.

true colours and luminosities of the stellar clusters (open squares) embedded in the SF regions, in a colour–magnitude diagram. We computed the true colours and luminosities from the dereddened ones using Eq. (2). The dereddened fluxes are adopted as the total broadband fluxes F_{total} in Eq. (2). The deviations between the crosses (colours and luminosities computed from the dereddened broadband total fluxes from the SF regions) and the open squares (the true colours and luminosities of cluster complexes embedded in the SF regions) in most cases are smaller than the absolute errors. In all these cases, the contribution of nebular emission is less than 40% of the total fluxes of the SF regions.

Some objects (No. 7b⁴, No. 18, No. 19, No. 22, No. 23, No. 28) show extremely high nebular emission fluxes, which are comparable with or even exceed the total fluxes of the SF regions at least in one of the $UBVR$ bands. According to the results of Reines et al. (2010), a nebular emission contribution which is greater than 80% of the total flux (Nos. 7b, 23) indicates an extremely young object ($t < 1$ Myr). From the other side, the true colours of objects Nos. 7b, 23 correspond to an age $t > 10$ Myr.

A contradiction between the extremely high contributions of nebular emission to the broadband fluxes, which correspond to very young ages ($t < 4$ Myr) (Reines et al. 2010), and considerable red $B - V$ indices, which correspond to older ages ($t > 10$ Myr), needs an explanation.

A possible cause of such a disagreement is a displacement between the photometric centres of the stars and those of the gas emissions, i.e. a displacement between a centre of photometric aperture and a centre of slit, which leads to a different light extinction for the stars than for the gas emissions. This results in wrong estimations of the colours of the star clusters, because the assumption that the stars and gas suffer from the same amount of extinction is not valid in such cases.

Fig. 13 shows that the stellar photometric centres of objects No. 9, No. 22 and No. 23 in NGC 2336, visible through the B band, are outside the slit. The centre of the slit lies in the gas emission photometric centre of the SF region, observed through the $H\alpha$ filter. The map of object No. 7 in Fig. 13 shows that slit ‘b’ crosses the edge of SF region No. 7, whereas slit ‘a’ crosses the centre of the

SF region. As a result, object No. 7b has an extremely red colour index $B - V$ (see Fig. 12) and a high contribution from nebular emission (95% in B). Object No. 7a has an ordinary colour index $B - V$ and a medium contribution from the nebular emission (11% in B).

Thus the spatial displacement between the photometric centres of the stars and of the gas emissions in SF regions such as No. 7b, No. 9, No. 22, and No. 23 leads to wrongly estimated extinction and overestimated contribution of nebular emission in the broad bands. Both lead to wrong colour–magnitude values of the star clusters.

SF regions such as No. 7b, No. 9, No. 22, and No. 23 in NGC 2336, discussed here, and similar objects in other galaxies, are excluded from the further analysis for the determination of the physical parameters of the star clusters, age and masses.

Objects Nos. 7b, 22, and 23 in NGC 2336 have unusual locations on another diagram, too (see Fig. 14). Object No. 9 in NGC 2336 shows an unreasonable value of its equivalent width $\text{EW}(H\alpha) > 1500\text{\AA}$ (one of the circles in Fig. 14). Object No. 22 in NGC 2336 shows an unreasonable ratio of fluxes $F(H\alpha)/F(R_{\text{stars}}) > 1$ (marked as a triangle in Fig. 14). Another two SF regions, No. 7b and No. 23 in NGC 2336, also have extremely high contributions in the U and B bands: 80% – 100% (No. 7b is marked as a triangle in Fig. 14, see also these objects in Fig. 12).

Further discussion of this problem will be continued below in Section 4.3.

4.3 $\text{EW}(H\alpha)$ and spectrophotometric fluxes

In Fig. 14, we compare the equivalent width $\text{EW}(H\alpha)$ with the ratio of the $H\alpha$ flux to the pure stellar emission flux in the R band for the studied objects. We get the equivalent widths $\text{EW}(H\alpha)$ from our spectroscopic observations presented in Gusev et al. (2012) and Gusev et al. (2013). The stellar emission fluxes $F(R_{\text{stars}})$ are derived from our R band photometry data, reduced for the light absorption and nebula emission contribution. In the cases of the three galaxies (NGC 628, NGC 6946, and NGC 7331), we used the available spectrophotometric $H\alpha$ fluxes (Table 3). For the other four galaxies, with unknown $H\alpha$ photometry, we corrected the absolute fluxes received through the slit, by a factor that accounts for the difference between the area of the round aperture, used by the photometry, and the area of the slit (for details see Section 3). Fig. 14 shows that most objects (black squares) are located in the left lower part of the diagram under the upper limits of the equivalent width $\text{EW}(H\alpha)$ (horizontal dot dashed line) and of the ratio of the $H\alpha$ flux to star emission flux in the R band (vertical dot dashed line), computed in Reines et al. (2010). These limits are appropriate for the youngest SF regions, with ages ~ 1 Myr. The distribution of these SF regions on the diagram (black squares) can be described by the following linear regression (solid line):

$$\log \text{EW}(H\alpha) = \log \frac{F(H\alpha)}{F(R_{\text{stars}})} + (3.15 \pm 0.05),$$

where the value of the constant 3.15 ± 0.05 is in good agreement with the effective bandwidth (1580\AA) of the R filter determined by Bessell (1990). The uncertainties of the values of $\text{EW}(H\alpha)$ are used as weights in the linear fitting. Dashed lines show the upper and lower 95% prediction limits of the linear fit, with a standard deviation of $\sigma = 0.37$ and a correlation coefficient of $r = 0.67$.

Four objects with unreasonable equivalent widths $\text{EW}(H\alpha) > 1500\text{\AA}$ (marked as circles) and nine objects with unreasonable ratios $F(H\alpha)/F(R_{\text{stars}}) > 1$ (marked as triangles) were not taken into account in the computation of the linear regression.

⁴ Object No. 7 is corrected for the gas contribution using the spectrum ‘b’ for this region.

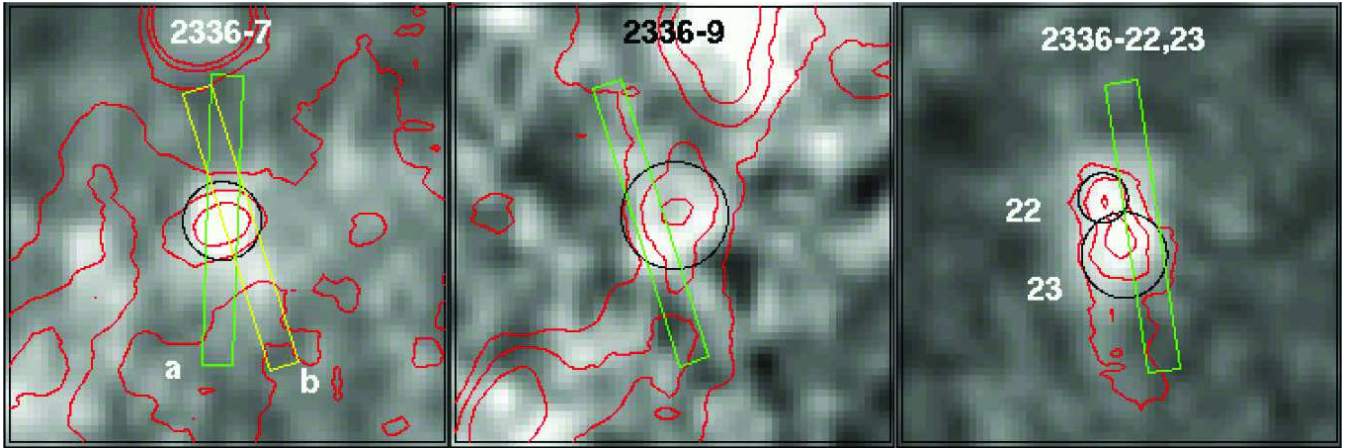


Figure 13. $H\alpha$ images of SF regions Nos. 7, 9, 22, and 23 in NGC 2336 with overlaid contours of isophotes in the B band. $H\alpha$ FITS image of NGC 2336 was taken from the NED (<http://ned.ipac.caltech.edu>; Epinat, Amram & Marcelin 2008). Circles show the position and size of apertures for the measurement of B and $H\alpha$ fluxes. Bars show the position of the slits during spectroscopic observations. The size of the images is 21.3×21.3 arcsec². North is upward and East is to the left. See the text for details.

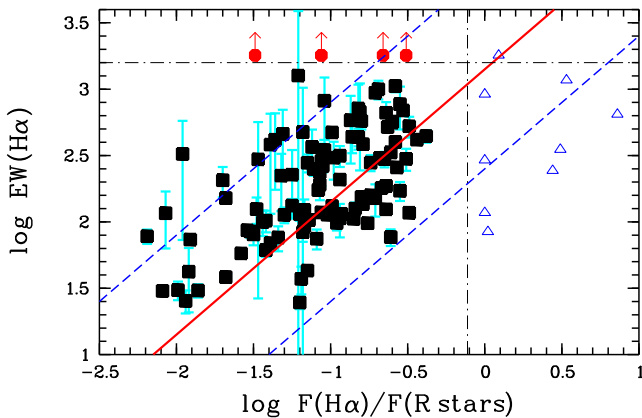


Figure 14. Diagram $\log F(H\alpha)/F(R_{\text{stars}})$ versus $\log EW(H\alpha)$ for the SF regions. Dot dashed lines are upper limits of the equivalent width $EW(H\alpha)$ (horizontal line) and of the ratio of the $H\alpha$ flux to star emission flux in the R band (vertical line), computed in Reines et al. (2010). The solid line is a linear fit, computed for SF regions (black squares), located under the upper limits of the $EW(H\alpha)$ and $F(H\alpha)/F(R_{\text{stars}})$ (horizontal and vertical dot dashed lines). Dashed lines are upper and lower 95% prediction limits of the linear fit. Circles show the SF regions with an unreasonable $EW(H\alpha) > 1500\text{\AA}$. SF regions with an unreasonable ratio $F(H\alpha)/F(R_{\text{stars}}) > 1$ are marked as triangles. See the text for details.

Most of these objects show either extremely blue or extremely red colours or even undeterminable true colours because of an unreasonably large contribution of the nebulosity emission, greater than the total flux in the used $UBVR$ broadbands (see Table 3). As noted above (see Section 4.2), the extreme characteristics of these objects may indicate a spatial deviation between the photometric centres of the $H II$ region and the star clusters associated with it. In such cases, the slit of the spectrograph crosses the centre of the $H II$ region, but covers the edge of the star cluster.

Such spatial separations were observed earlier by Maíz-Apellániz et al. (1998). A two-dimensional spectrophotometric map of the central region of NGC 4214, obtained by Maíz-Apellániz et al. (1998), shows that the stars, gas, and dust

clouds in the brightest SF regions are spatially separated. The dust is concentrated at the edges of the region of ionisation and primarily influences the nebular emission lines, whereas the stellar continuum is located in a region that is relatively free from dust and gas. Thus, the assumption about $A(\text{stars}) = A(\text{Balmer})$, adopted here, is not valid in such SF regions. This leads to wrong colours for the star clusters embedded in such SF regions. We excluded abnormal objects from further analysis when determining the physical parameters of the star clusters embedded in the SF regions. In Fig. 13 and Fig. 15 we present maps of the SF regions which are marked by the triangles and circles in Fig. 14. Fig. 13 shows that the centre of the ionised gas cloud lies at the edge of the star forming region (the slit is located in the photometric centre, visible through the $H\alpha$ filter) and there are no stars or a very small number of stars that can make a significant contribution to the continuum emission observed through the slit. The photometric centre, observed through the B filter, lies outside the slit's area.

A special case is object No. 38 in NGC 6946 (Fig. 15). It has an extremely high $EW(H\alpha) > 1500\text{\AA}$ and an unreasonably low $A_V < A(V)_{\text{Gal}}$. The object also has maximum deviation from the one-to-one line in Fig. 10. Possibly, it was incorrectly identified.

4.4 Twice observed objects

Among the studied SF regions there is a set of objects that were observed twice. In these cases, we took weighted averages of the measured metallicities, absorptions, $EW(H\alpha)$ s, and U , B , V , R , and I fluxes. For each measurement, 'a' and 'b', of the twice observed SF regions, we calculated the weights in the following way: $p_a = F(H\beta)_a / (F(H\beta)_a + F(H\beta)_b)$ and $p_b = F(H\beta)_b / (F(H\beta)_a + F(H\beta)_b)$. Here $F(H\beta)_a$, $F(H\beta)_b$ are non-reddened fluxes in the $H\beta$ line of the spectra 'a', 'b', taken from Gusev et al. (2012) and Gusev et al. (2013). This procedure was followed for 10 out of the 12 measurement pairs for which both measurements, 'a' and 'b', showed no extremely high nebular emission contribution ($< 40\%$) and $EW(H\alpha) < 1500\text{\AA}$.

Regions No. 7b in NGC 2336 and No. 8b in NGC 6946 have extremely high nebular contributions $> 50\%$ in every passband, and unreasonable ratios $F(H\alpha)/F(R_{\text{stars}}) > 1$ (see Sections 4.2 and 4.3). We excluded these objects from further consideration. In the case

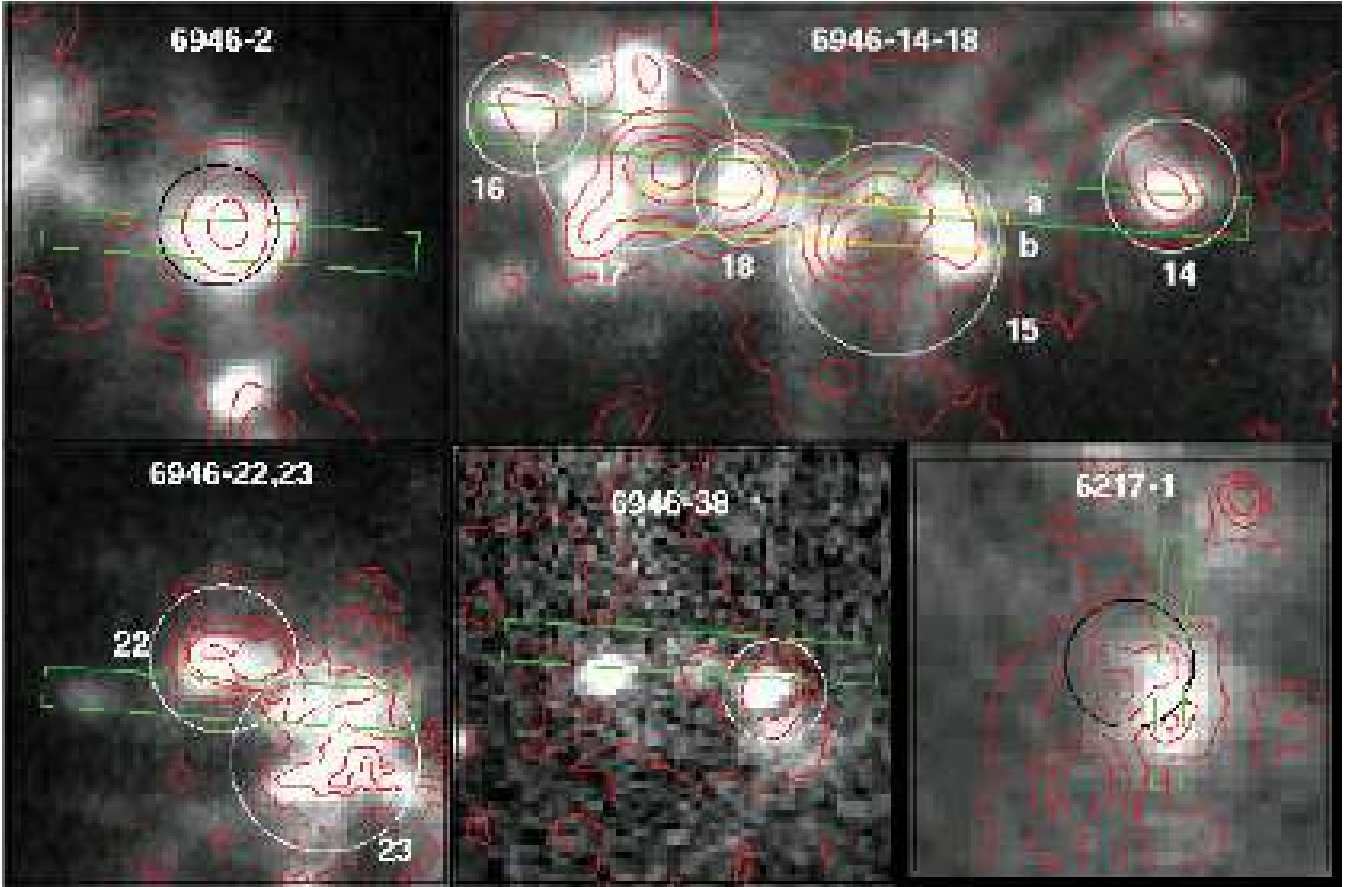


Figure 15. Same as Fig. 13, but for SF regions Nos. 2, 14–18, 22, 23, and 38 in NGC 6946 and No. 1 in NGC 6217. The letters ‘a’ and ‘b’ indicate the position of the slits for the measurement of the spectra of objects Nos. 14 and 15a and Nos. 15b and 18, respectively. The size of the images is $16.5 \times 16.5 \text{ arcsec}^2$ or $33.1 \times 16.5 \text{ arcsec}^2$ for the areas in NGC 6946 and $23.3 \times 23.3 \text{ arcsec}^2$ for the area in NGC 6217. North is upward and East is to the left. See the text for details.

of objects No. 7 in NGC 2336 and No. 8 in NGC 6946, we assume the photometric and spectroscopic quantities obtained for objects No. 7a in NGC 2336 and No. 8a in NGC 6946.

5 COMPARISON WITH MODELS

Here we compare the observed photometric properties of the SF regions with a numerical SSP-model, with an underlying Salpeter IMF, valid within a stellar mass range below m_{up} and above m_{low} .

Since the range of the SF region’s masses varies from $10^4 M_{\odot}$ up to $10^7 M_{\odot}$, we constructed models in *Standard* modes according to the technique described in Piskunov et al. (2011). The standard mode reproduces the features of standard SSP models with a continuously populated IMF, whereas the extended mode takes into account the effect of a randomly populated IMF. As shown by Piskunov et al. (2009), the effect of the randomly populated discrete IMF plays an important role in comparing colours of low mass clusters ($M_{\text{cl}} < 10^4 M_{\odot}$) with the synthetic colours of models.

We used a grid of isochrones provided by the Padova group (Bertelli et al. 1994; Girardi et al. 2000; Marigo & Girardi 2007; Marigo et al. 2008) via the online server CMD⁵. We used the prior sets of stellar evolutionary tracks (version 2.3), described in

Marigo et al. (2008), instead of the latest Padova models (version 2.5), described in Bressan et al. (2012), because the latest version 2.5 is computed for a narrower interval of initial masses, ranging from $0.1 M_{\odot}$ to $12 M_{\odot}$, while for our purposes we need the interval of initial masses to reach up to $100 M_{\odot}$.

As we discussed previously in Gusev, Egorov & Sakhibov (2014), the multiple structure of unresolved star forming complexes does not affect their integrated $B - V$ colour indices and thereby the results of the estimations of the age of a YMC. Since we use the integrated B luminosities and integrated $B - V$ colours of unresolved star complexes in the CMD, we can assign the parameters of the model of a single massive cluster to the unresolved multiple star clusters.

In Fig. 16 (left panel) we show the observed (not dereddened, not corrected for the impact of nebular emission) $B - V$ colours versus M_B luminosities of the star forming regions in the studied galaxies. Fig. 16 also shows the evolutionary tracks of the SSP models. The models younger than 10 Myr are shown as black thick lines, the models between 10 Myr and 1.5 Gyr are shown as grey lines. We do not show SF regions with extremely high nebular emission contributions $> 40\%$ in the B and/or V passbands (see Section 4.2), regions with $\text{EW}(\text{H}\alpha) > 1500 \text{ \AA}$, and objects with unreasonable ratios $F(\text{H}\alpha)/F(R_{\text{stars}}) > 1$ (see Section 4.3) in this figure.

Because all the objects in the left panel of Fig. 16 are located in the unreal age interval between 400 Myr and 1.5 Gyr, a light ab-

⁵ <http://stev.oapd.inaf.it/cgi-bin/cmd>

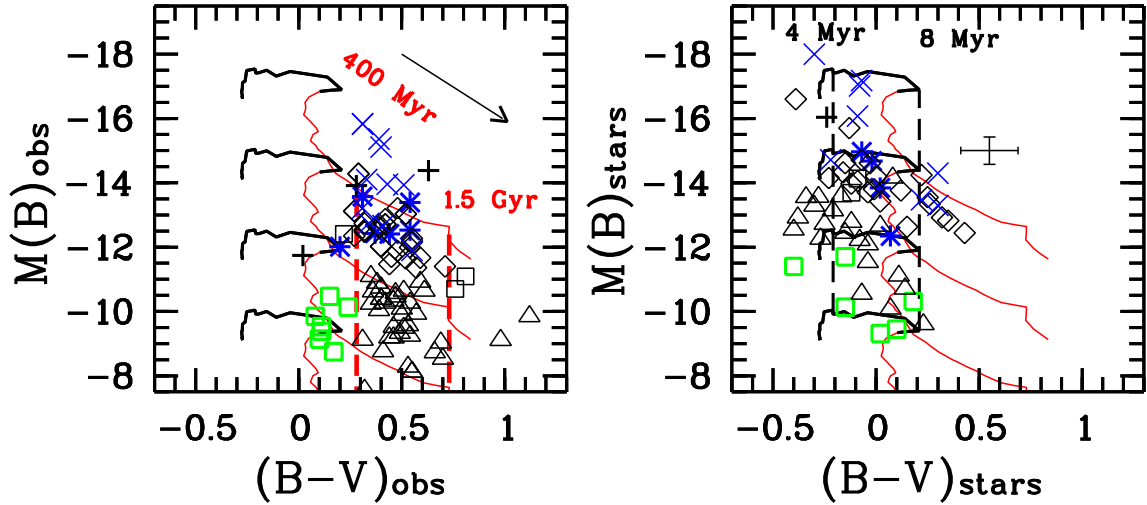


Figure 16. Observed (left) and true (right) colours and luminosities of SF regions in studied galaxies compared to SSP models. Grey squares: NGC 628, stars: NGC 783, rhombuses: NGC 2336, crosses (+): NGC 6217, triangles: NGC 6946, black squares: NGC 7331, crosses (×): NGC 7678. The big cross in the right panel indicates the mean of the absolute error of true colour–magnitude values. Evolutionary tracks for the models with Salpeter’s IMF and $Z = 0.012$ are shown. See the text for details.

sorption correction is needed. Remember that all our objects contain giant H II regions ionised by massive star clusters younger than 10 Myr. Fig. 16 shows that the extinction vector is parallel to the evolution tracks for 400 Myr and 1.5 Gyr. This is a clear demonstration of how ‘age–absorption’ degeneracy works. To avoid the degeneracy problem, we use the dereddening method based on the independent measurements of the Balmer decrements (see Section 4).

In Fig. 16 (right panel) we compare the true colours and luminosities, which are corrected for light extinction and impact of nebular emission of star clusters (cluster complexes), with SSP models (black and grey lines) in the colour–magnitude diagram. As we noted above (Section 1), we call the colours and luminosities which are unaffected by both the extinction and the nebula emission to broad bands the ‘true’ colours and luminosities of the young massive cluster complexes.

We eliminated from Fig. 16 (right panel) the objects with large errors of A_V estimations ($\Delta A_V > 0.8$ mag), as well as the objects with underestimated or overestimated light extinction, with extremely red or blue $B - V$ indices. An example of one of the two objects with underestimated extinction, No. 1 in NGC 6217, is shown in Fig. 15. Most of objects with overestimated light extinction are SF regions in NGC 6946 (see Table 4). For example, we discuss three ‘abnormal’ objects, Nos. 2, 17, and 22 in NGC 6946 (triangles). These objects have extremely blue $B - V$ colour indices, which cannot be fitted by the youngest models of star clusters. At the same time, the low relative contributions of the nebular emission to the U , B , V fluxes indicate older ages $t > 5$ Myr, according to Starburst99 model evolutionary isochrones for the nebular continuum presented in Reines et al. (2010). Note that the light absorption estimates for all three objects are extremely high: $A_V = 3.84$, 3.86 , and 4.59 mag, respectively, while the characteristic value of the light absorption for SF regions in NGC 6946 is $A_V = 2.2 \pm 0.9$ mag. This could indicate a possible overestimation of the light absorption of the stellar continuum observed through $UBVRI$ filters. Note that the estimations of light absorption are based on the observed Balmer decrement values under the assumption

that the emission from stars embedded in the SF region is absorbed in the same way as the emission in the lines of ionised hydrogen surrounding the star clusters in the SF region. This is valid when the clumping of the gas and dust distribution in the space of the star forming complex is not high, otherwise the light extinction of the stars is not equal to the light extinction of the emission of ionised gas. It seems to us that this is exactly what happens in the three abnormal objects, Nos. 2, 17, and 22. Fig. 15 shows the displacements between the photometric centres in these objects, visible through the B and $H\alpha$ filters. The case of object No. 22 can be explained as a displacement between the gas cloud and the star clusters along the radial direction.

Fig. 16 (right panel) shows that most of the objects are in a narrow age interval ($t < 8$ Myr). This result agrees with the time interval determined by the life time of the giant H II regions. The big cross indicates the mean of the absolute error of true colour–magnitude values. The displacements of most objects from the model’s area lie within the error interval.

There are 5 objects in distant galaxies NGC 2336 (three rhombuses), NGC 7678 (two crosses ‘×’), which are located outside of the area of the young models ($t < 10$ Myr), and can be fitted with older models between 300 Myr and 700 Myr. As the sizes of all 5 objects belong to the range from 300 pc to 600 pc, they are cluster complexes. As the evolutionary tracks for greater ages ($t > 50$ Myr) are parallel to a ‘reddening vector’, we meet the well known age–absorption degeneracy in the case of these 5 cluster complexes. There are two possible interpretations.

First, a possible spatial displacement between the photometric centres of the nebular emission and stellar continuum provides a spatially inhomogeneous extinction, so our assumption that the stars and gas suffer from the same amount of extinction is invalid here. In the case of these 5 cluster complexes, it could be evidence for an underestimation of the light extinction and $A_V(\text{stars}) > A_V(\text{Balmer})$.

Second, near young clusters, which ionize the gas in the SF region, there are clusters with older stellar populations. The large

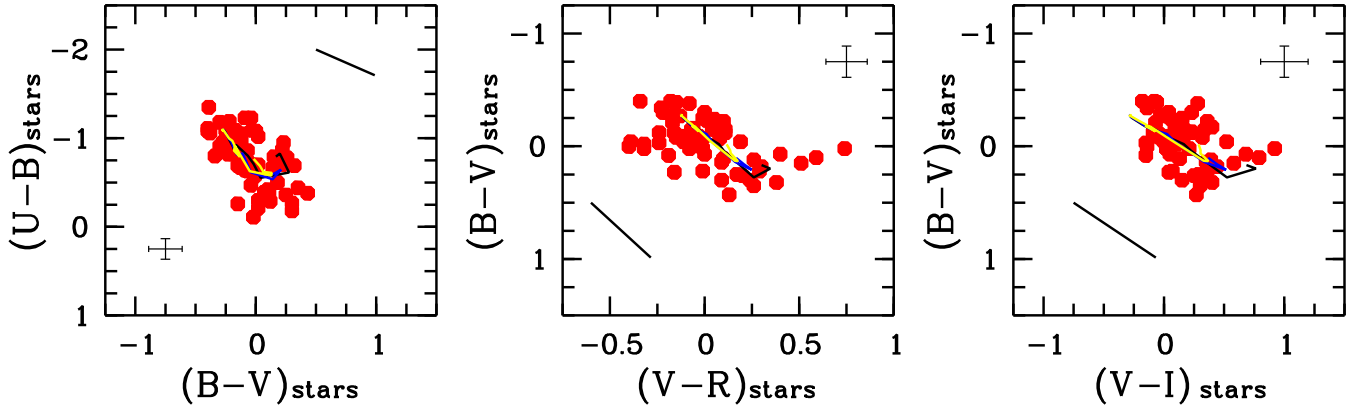


Figure 17. Colour-colour diagrams $(U-B)-(B-V)$, $(B-V)-(V-R)$, and $(B-V)-(V-I)$ for the true colours of cluster complexes in the studied galaxies. Black lines show SSP models with continuously populated IMF with Salpeter's slope $\alpha = -2.35$ and $Z = 0.019$, grey lines show models with $Z = 0.012$, and light lines show models with $Z = 0.008$. The SF regions with estimated ages and masses are shown as grey circles. The error crosses in the diagrams show the mean accuracy of the colours of these objects. The black straight line in the corner of the diagrams is parallel to the extinction vector.

sizes of these 5 objects can also indicate a possible coexistence of old and extremely young star clusters in the same SF region.

On the other hand, the deviations of these 5 objects from the area of the young models ($t < 10$ Myr) do not exceed the errors of the photometric properties. In Section 6, these objects are fitted with young models (see Table 4).

Fig. 17 plots SSP model tracks for the two-colour diagrams. The true colours, derived for our star forming regions, are superimposed on these diagrams. The offsets between the positions of the SF regions and the theoretical tracks are comparable with the mean accuracy of the derivations of the true colours, shown as big crosses on the diagrams.

The true magnitudes and colours of the SF regions, which are shown in Figs. 16 (right panel) and 17, are given in Table A1.

6 PHYSICAL PARAMETERS OF THE STAR FORMING REGIONS

Multicolour photometry provides a useful tool for constraining the physical parameters of YMC complexes in star forming regions. Here we use the method of the minimisation of $O-C$ parameters (observed minus computed):

$$O-C = [[(U-B)_{\text{obs}} - (U-B)_{\text{model}}]^2 + [(B-V)_{\text{obs}} - (B-V)_{\text{model}}]^2 + [M_{\text{obs}}(B) - M(B)_{\text{model}}]^2]^{1/2}$$

to constrain the ages and masses of the YMC complexes in the star forming regions. Under the concept of ‘observed parameters’ we place the true colours and luminosities, which are those corrected for the light extinction and the impact of nebular emission. The procedure for finding the values of the physical parameters, ages (t) and YMC’s masses (m_{cl}) can be subdivided into the following steps. First, the models of stellar population, computed for the derived (from spectroscopy) chemical abundance, are presented in the form of a grid of colour indices and luminosities for a broad range of variation of searching parameters $t(i)$ and $m_{\text{cl}}(j)$. Here, the indices i, j are the numbers of rows and columns in a two dimensional grid of photometric parameters. The table step of the $\log(t)$

parameter variation is 0.05 dex. The table step of the $\log(m_{\text{cl}})$ parameter variation depends on the interval of luminosity variations of YMC complexes in a given galaxy:

$$h_{\log(m_{\text{cl}})} = \frac{\log(m_{\text{cl}}(\text{max})) - \log(m_{\text{cl}}(\text{min}))}{N},$$

where N is the number of the evolutionary tracks. For every node (i, j), we calculated the value of the $(O-C)_{i,j}$ parameter.

The second step is the search for the grid node in which the $(O-C)_{i,j}$ parameter has a minimum value. We accept corresponding values $t = t(i)$, $m_{\text{cl}} = m_{\text{cl}}(j)$ as a solution of the problem for a given individual young massive cluster or cluster complex. The ages and masses of YMC complexes, computed through the minimization of the $O-C$ parameters (observed minus computed), are presented in columns (7) and (8) of Table 4. The uncertainty introduced through the light absorption correction and accounting for a gas emission contribution is the source of the rather low accuracies of the age estimations, especially for very small ages ($t < 3$ Myr), where the colour gradients of age are very steep. In Table 4 we present the errors of the ages and masses computed according to Gauss’s law of error propagation.

In the assessment of the ages and masses, we did not use the $V-R$ and $V-I$ colour indices because, in the case of YMCs, the R and I fluxes are weakly sensitive to changes in age, and the actual observational errors lead to large uncertainties.

We estimated the ages for 57 and masses for 63 YMC complexes of 102 observed SF regions. We believe that the condition $A(\text{Balmer}) = A(\text{stars})$ is valid for these regions. The estimates of the ages for 6 objects have been obtained with low accuracies, the errors of the age estimation exceeding the range of ages of 1–8 Myr.

The left histogram in Fig. 18 shows the age frequency distribution of 57 SF regions in studied galaxies. The mean value of the ages for our sample is 5.5 ± 2.1 Myr. The drastic decay of the number of YMC complexes between 8 and 10 Myr is in agreement with the lifetime estimates of H II regions. The relatively small number of YMC clusters with ages < 4 Myr can be explained by the effect of selection: very young clusters/complexes have a high extinction. During the first 3–4 Myr of life of a YMC, its absorption decreases from $A_V \sim 10$ mag to ≈ 1 mag, while its luminosity increases in-

Table 4. The physical parameters of the star forming regions.

H II region	r (kpc)	r/R_{25}	A_V (mag)	EW(H α) (Å)	Z	$I_B(\text{gas})/$ $I_B(\text{total})$	t (Myr)	m/M_\odot ($10^4 M_\odot$)	d (pc)	Structure ^a	Notes ^b
1	2	3	4	5	6	7	8	9	10	11	12
NGC 628											
1	4.55	0.415	1.58 ± 0.67	476^{+550}_{-476}	—	0.05	$2.0^{+6.1}_{-2.0}$	6.50 ± 1.02	65	dbl	
2	3.11	0.283	1.24 ± 0.51	102 ± 19	—	0.05	6.3 ± 2.6	5.00 ± 1.17	130	dbl, pt	
3	2.58	0.235	0.70 ± 0.45	583 ± 308	—	0.28	—	1.21 ± 0.06	70	st	
4	2.77	0.253	0.79 ± 0.67	296 ± 269	0.0043 ± 0.0017	0.05	6.3 ± 0.4	1.25 ± 0.23	110	st	
5	1.34	0.122	0.64 ± 0.54	> 1500	—	0.12	—	—	115	dbl	2
6	1.51	0.138	1.81 ± 2.05	25 ± 5	—	0.01	—	—	90	dbl	5
7	4.01	0.366	0.00 ± 0.28	674 ± 430	0.0106 ± 0.0014	0.43	—	—	130	ring	1
8	5.31	0.484	0.26 ± 0.26	716 ± 365	0.0091 ± 0.0011	0.32	7.9 ± 1.4	1.00 ± 0.06	75	st, pt	
9	5.42	0.494	1.86 ± 0.28	> 1500	0.0082 ± 0.0013	0.58	—	—	45	st	1, 3
10	6.25	0.571	0.06 ± 0.47	305 ± 97	0.0087 ± 0.0018	0.20	6.3 ± 0.9	1.45 ± 0.20	220	compl	
NGC 783											
1	10.60	0.729	0.60 ± 0.32	151 ± 41	0.0068 ± 0.0010	0.34	6.3 ± 1.9	10.0 ± 2.2	750	dif, pt	
2	12.83	0.881	0.17 ± 1.17	42 ± 21	—	0.03	—	—	1000	ring	5
3	8.33	0.572	1.09 ± 0.19	299 ± 57	0.0120 ± 0.0009	0.26	—	91.2 ± 16.9	1300	dif	
4	11.96	0.822	1.92 ± 0.42	43 ± 4	0.0075 ± 0.0014	0.09	5.6 ± 0.1	95.5 ± 52.9	550	dif	
5	10.17	0.699	1.30 ± 0.21	172 ± 28	—	0.25	6.3 ± 2.9	38.0 ± 6.9	500	st, pt	
6	11.15	0.766	0.94 ± 0.19	244 ± 39	0.0088 ± 0.0007	0.76	—	—	550	st, pt	1, 3
7	12.20	0.838	1.63 ± 0.96	25 ± 3	0.0062 ± 0.0025	0.09	—	—	550	st	5
8	8.42	0.578	1.56 ± 0.19	1170^{+1238}_{-1170}	0.0122 ± 0.0012	0.37	—	—	650	st	1, 3
NGC 2336											
1	20.79	0.885	0.43 ± 0.22	140 ± 59	0.0056 ± 0.0006	0.07	10.0 ± 1.1	47.4 ± 5.7	630	dbl	
2	16.89	0.719	0.96 ± 0.17	348 ± 66	0.0098 ± 0.0008	0.17	6.3 ± 2.9	34.2 ± 5.3	730	dif	
3	11.30	0.481	1.47 ± 0.34	98 ± 12	0.0133 ± 0.0021	0.12	5.0 ± 1.1	47.4 ± 17.7	390	dif	
4	7.79	0.331	0.87 ± 0.27	114 ± 18	—	0.13	7.9 ± 1.3	84.1 ± 11.0	520	dif	
5	4.86	0.207	0.73 ± 0.68	31 ± 5	—	0.03	7.9 ± 0.8	24.6 ± 6.8	370	dif	
6	23.02	0.979	2.39 ± 0.13	437 ± 66	0.0047 ± 0.0004	0.13	—	—	470	st, pt	6
7	15.19	0.646	0.98 ± 0.32	416 ± 241	0.0090 ± 0.0014	0.11	8.9 ± 0.7	19.3 ± 2.5	470	dif	
8	12.99	0.553	0.68 ± 0.15	113 ± 8	0.0124 ± 0.0008	0.18	7.1 ± 2.7	31.5 ± 3.3	390	st	
9	10.27	0.437	0.23 ± 0.17	> 1500	0.0190 ± 0.0015	0.43	—	—	460	dif	1, 2
10	11.82	0.503	1.21 ± 0.12	135 ± 8	0.0129 ± 0.0006	0.13	5.0 ± 0.1	71.4 ± 11.1	420	st	
11	10.59	0.451	1.92 ± 0.30	287 ± 101	0.0077 ± 0.0010	0.11	—	60.6 ± 12.7	330	dif	
12	8.22	0.349	1.99 ± 0.55	58 ± 5	—	0.04	5.6 ± 0.6	92.2 ± 51.2	550	dif, pt	
13	14.84	0.632	2.62 ± 0.17	279 ± 43	0.0218 ± 0.0025	0.07	—	552 ± 169	810	dif	
14	22.83	0.971	1.51 ± 0.13	141 ± 9	0.0058 ± 0.0003	0.17	4.5 ± 1.0	77.5 ± 7.9	480	st	
15	18.49	0.787	0.20 ± 0.27	123 ± 25	0.0063 ± 0.0008	0.08	6.3 ± 2.4	15.1 ± 3.0	580	dif, pt	
16	12.11	0.515	1.25 ± 0.14	122 ± 8	0.0101 ± 0.0007	0.22	7.1 ± 4.7	29.0 ± 3.9	730	dbl	
17	14.05	0.598	1.23 ± 0.11	189 ± 12	0.0122 ± 0.0006	0.20	6.3 ± 0.6	190 ± 36	860	st, pt	
18	17.18	0.731	2.82 ± 0.81	117 ± 30	—	> 1	—	—	430	st	1, 3, 5
19	13.13	0.559	1.52 ± 0.30	84 ± 8	0.0093 ± 0.0012	0.43	—	—	450	dif	1, 3
20	14.49	0.616	2.26 ± 0.28	98 ± 2	0.0107 ± 0.0012	0.16	—	51.4 ± 13.3	320	st, pt	
21	13.50	0.574	0.75 ± 0.26	237 ± 91	0.0124 ± 0.0014	0.18	7.1 ± 3.5	11.8 ± 1.7	270	dif, pt	
22	17.88	0.761	1.04 ± 0.11	916 ± 207	0.0091 ± 0.0004	> 1	—	—	320	st, pt	1, 3
23	17.47	0.743	0.19 ± 0.08	443 ± 48	0.0086 ± 0.0004	0.83	—	—	380	st, pt	1
24	15.61	0.664	1.79 ± 0.54	75 ± 13	0.0067 ± 0.0015	0.09	3.5 ± 2.1	37.1 ± 19.8	560	dif, pt	
25	15.32	0.652	1.84 ± 0.36	1267^{+2610}_{-1267}	0.0074 ± 0.0012	0.07	$3.5^{+4.2}_{-3.5}$	65.8 ± 28.5	520	dif, pt	
26	12.43	0.529	1.97 ± 0.68	77 ± 11	0.0082 ± 0.0023	0.21	—	43.7 ± 18.2	260	dif, pt	
27	12.88	0.548	1.07 ± 0.54	76 ± 16	0.0071 ± 0.0017	0.07	5.6 ± 0.4	34.2 ± 16.5	510	dif, pt	
28	20.17	0.858	0.17 ± 0.11	297 ± 40	0.0081 ± 0.0005	0.57	—	—	420	ring	1
NGC 6217											
1	3.30	0.479	0.21 ± 0.21	74 ± 5	0.0128 ± 0.0012	0.05	—	—	495	dbl, pt	6
2	4.41	0.640	1.63 ± 0.67	78 ± 10	—	0.01	2.5 ± 2.4	448 ± 293	300	dbl, pt	
3	3.24	0.471	1.71 ± 0.54	461 ± 239	0.0078 ± 0.0018	0.05	—	—	185	st	6
NGC 6946											
1	5.34	0.402	2.69 ± 0.26	437 ± 108	0.0123 ± 0.0013	0.12	—	—	60	st	6

^a compl: complex structure (more than three separated objects); dbl: double object; dif: separated object with diffuse profile; pt: brighter part (core) of an extended star forming region; ring: ring structure; st: separated object with star-like profile; tr: triple object

^b 1: objects with $I(\text{gas})/I(\text{total}) > 40\%$ in the B and/or V ; 2: objects with $\text{EW}(\text{H}\alpha) > 1500\text{\AA}$; 3: objects with $F(\text{H}\alpha)/F(R_{\text{stars}}) > 1$; 4: an object lacking any photometry; 5: objects with $\Delta A_V > 0.8$ mag; 6: objects for which, apparently, the condition $A(\text{stars}) = A(\text{Balmer})$ is not satisfied.

Table 4. Continued

H II region	r (kpc)	r/R_{25}	A_V (mag)	EW(H α) (Å)	Z	$I_B(\text{gas})/$ $I_B(\text{total})$	t (Myr)	m/M_\odot ($10^4 M_\odot$)	d (pc)	Structure ^a	Notes ^b
1	2	3	4	5	6	7	8	9	10	11	12
NGC 6946											
2	6.51	0.490	3.84 ± 0.08	519 ± 25	0.0088 ± 0.0003	0.14	—	—	110	dif	6
3	3.99	0.300	1.16 ± 0.73	107 ± 30	—	0.15	7.9 ± 1.7	1.24 ± 0.14	135	ring	
4	1.75	0.131	0.41 ± 0.19	106 ± 8	—	0.41	—	—	90	dif	1
5	1.91	0.144	1.54 ± 0.36	68 ± 6	—	0.05	7.1 ± 2.1	1.24 ± 0.13	110	dif	
6	2.95	0.222	1.92 ± 0.15	92 ± 4	0.0118 ± 0.0008	0.07	4.5 ± 0.5	18.4 ± 2.3	180	compl	
7	2.14	0.161	3.35 ± 1.53	37 ± 9	—	0.04	—	—	45	dif, pt	5
8	2.21	0.166	1.93 ± 0.09	151 ± 11	0.0108 ± 0.0005	0.04	7.1 ± 2.2	3.28 ± 0.19	115	dif, pt	
9	2.28	0.171	2.37 ± 0.11	939 ± 77	0.0047 ± 0.0004	0.19	3.2 ± 2.6	22.8 ± 2.3	150	dbl, pt	
10	2.75	0.207	2.05 ± 0.15	118 ± 6	0.0325 ± 0.0022	0.10	5.6 ± 0.3	14.8 ± 1.4	80	dbl, pt	
11	3.32	0.250	1.97 ± 0.15	577 ± 80	0.0295 ± 0.0011	0.21	5.6 ± 0.2	8.65 ± 0.65	65	st, pt	
12	3.13	0.236	2.39 ± 0.13	174 ± 9	—	0.08	4.5 ± 2.0	28.3 ± 2.9	135	dif, pt	
13	3.12	0.235	2.95 ± 0.15	264 ± 28	0.0160 ± 0.0010	0.10	2.5 ± 0.5	14.8 ± 1.2	40	st, pt	
14	3.87	0.291	3.35 ± 0.11	998 ± 160	0.0147 ± 0.0007	0.16	—	—	65	dif	6
15	3.98	0.299	2.15 ± 0.15	622 ± 122	0.0151 ± 0.0012	0.25	$1.3 \pm_{1.3}^{5.2}$	31.6 ± 1.1	145	dbl, pt	
16	4.34	0.326	3.76 ± 0.15	664 ± 135	0.0161 ± 0.0010	0.20	—	—	65	dbl	6
17	4.22	0.318	3.86 ± 0.13	385 ± 27	0.0175 ± 0.0009	0.11	—	—	70	st, pt	6
18	4.12	0.310	1.35 ± 0.13	180 ± 12	0.0041 ± 0.0003	0.29	10.0 ± 0.5	4.06 ± 0.09	55	st, pt	
19	5.00	0.376	2.99 ± 0.11	1055 ± 107	0.0110 ± 0.0005	0.18	—	—	125	dbl	6
20	4.81	0.362	2.28 ± 0.15	> 1500	0.0063 ± 0.0004	0.20	—	—	90	dif	1
21	5.14	0.387	2.26 ± 0.11	570 ± 55	0.0109 ± 0.0005	0.22	—	—	125	dif, pt	6
22	6.44	0.485	4.59 ± 0.13	304 ± 14	0.0090 ± 0.0008	0.09	—	—	75	dbl, pt	6
23	6.41	0.483	2.71 ± 0.13	334 ± 29	0.0110 ± 0.0006	0.26	—	—	85	dif, pt	6
24	2.35	0.177	0.39 ± 0.96	30 ± 4	—	0.06	—	—	65	st, pt	5
25	3.38	0.254	2.56 ± 0.13	417 ± 35	0.0116 ± 0.0006	0.21	—	—	200	tr	6
26	4.92	0.371	1.60 ± 0.11	159 ± 6	0.0072 ± 0.0003	0.22	4.5 ± 0.7	9.63 ± 0.86	120	dbl, pt	
27	4.72	0.356	2.31 ± 0.08	691 ± 47	0.0079 ± 0.0003	0.20	—	—	145	st, pt	6
28	5.10	0.384	2.54 ± 0.41	113 ± 15	0.0064 ± 0.0011	0.05	3.5 ± 3.1	28.3 ± 9.3	100	st, pt	
29	4.95	0.373	1.81 ± 0.32	115 ± 12	—	0.13	5.6 ± 0.3	6.97 ± 1.24	225	compl	
30	6.00	0.452	2.37 ± 0.08	560 ± 15	0.0057 ± 0.0003	0.30	$1.1 \pm_{1.1}^{4.4}$	83.3 ± 2.0	215	tr, pt	
31	6.47	0.487	1.26 ± 0.17	316 ± 57	0.0059 ± 0.0005	0.15	6.3 ± 0.3	1.91 ± 0.13	80	ring, pt	
32	6.35	0.478	2.67 ± 0.17	132 ± 8	0.0063 ± 0.0005	0.08	$2.0 \pm_{2.0}^{6.1}$	22.8 ± 1.1	80	dif, pt	
33	2.47	0.186	1.66 ± 0.41	292 ± 96	0.0113 ± 0.0020	> 1	—	—	65	st, pt	1, 3
34	2.16	0.162	2.22 ± 0.13	209 ± 15	0.0177 ± 0.0009	0.11	3.5 ± 1.5	6.97 ± 0.63	100	dbl, pt	
35	0.43	0.032	3.35 ± 0.36	38 ± 2	—	0.03	7.1 ± 2.1	54.1 ± 18.0	80	dbl	
36	3.10	0.234	1.39 ± 0.15	117 ± 6	0.0148 ± 0.0009	0.38	6.3 ± 1.0	4.06 ± 0.33	155	tr, pt	
37	2.88	0.217	1.64 ± 0.62	84 ± 13	—	0.08	6.3 ± 0.7	12.0 ± 4.3	225	ring, pt	
38	5.29	0.398	0.54 ± 0.17	> 1500	0.0162 ± 0.0013	0.13	—	—	55	st	2
39	4.30	0.323	2.67 ± 0.11	400 ± 21	0.0126 ± 0.0005	0.17	—	—	80	st, pt	6
NGC 7331											
1	9.78	0.488	0.19 ± 0.60	55 ± 13	0.0070 ± 0.0019	—	—	—	90	dif, pt	4
2	5.45	0.272	3.27 ± 1.45	30 ± 2	—	0.01	—	—	225	tr	5
3	3.48	0.173	2.65 ± 0.36	382 ± 168	0.0057 ± 0.0013	0.05	4.0 ± 0.5	50.2 ± 16.4	110	st	
4	9.06	0.451	1.07 ± 0.17	251 ± 28	0.0090 ± 0.0006	0.11	5.0 ± 1.2	35.2 ± 4.5	410	compl	
NGC 7678											
1	13.02	0.901	2.01 ± 1.09	227 ± 121	0.0059 ± 0.0025	0.08	—	—	300	st	5
2	8.57	0.593	0.68 ± 0.45	223 ± 103	0.0084 ± 0.0016	0.08	7.1 ± 1.0	32.9 ± 8.6	590	st	
3	8.10	0.560	0.30 ± 0.21	367 ± 128	0.0040 ± 0.0006	0.16	8.9 ± 2.8	90.6 ± 13.8	620	dif	
4	8.11	0.561	0.64 ± 0.17	819 ± 405	0.0090 ± 0.0008	0.24	—	—	520	st	6
5	8.15	0.564	0.13 ± 0.41	100 ± 22	0.0119 ± 0.0021	0.08	7.1 ± 4.0	30.0 ± 10.4	430	st	
6	7.02	0.486	1.64 ± 0.30	69 ± 5	0.0091 ± 0.0011	0.05	5.6 ± 0.2	274 ± 148	450	dif, pt	
7	9.63	0.666	1.47 ± 0.11	191 ± 9.0	0.0074 ± 0.0003	0.11	4.0 ± 0.8	627 ± 190	740	dif	
8	8.56	0.592	1.71 ± 0.08	330 ± 10	0.0086 ± 0.0003	0.17	2.2 ± 2.2	2740 ± 340	790	dbl	
9	11.87	0.821	1.69 ± 0.15	280 ± 39	0.0093 ± 0.0006	0.21	$1.6 \pm_{1.6}^{3.6}$	157 ± 14	460	st	
10	5.56	0.384	1.52 ± 0.11	104 ± 5	0.0080 ± 0.0004	0.09	5.6 ± 0.4	627 ± 188	490	st, pt	

^a compl: complex structure (more than three separated objects); dbl: double object; dif: separated object with diffuse profile; pt: brighter part (core) of an extended star forming region; ring: ring structure; st: separated object with star-like profile; tr: triple object

^b 1: objects with $I(\text{gas})/I(\text{total}) > 40\%$ in the B and/or V ; 2: objects with $\text{EW}(\text{H}\alpha) > 1500\text{\AA}$; 3: objects with $F(\text{H}\alpha)/F(R_{\text{stars}}) > 1$; 4: an object lacking any photometry; 5: objects with $\Delta A_V > 0.8$ mag; 6: objects for which, apparently, the condition $A(\text{stars}) = A(\text{Balmer})$ is not satisfied

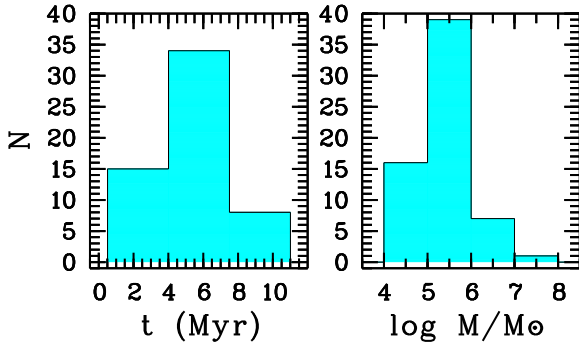


Figure 18. Frequency distribution of ages (left panel) and masses (right panel) of star complexes in all studied galaxies.

significantly (see Whitmore et al. 2011, and references therein; see also the evolutionary tracks in Fig. 16). As a result, the apparent magnitude of a YMC of the same mass will be maximal for ages 4 – 7 Myr.

The distances to the studied galaxies range from 7 Mpc up to 70 Mpc. As a result, we observe different absolute fluxes and different mass intervals for the YMC complexes in the different galaxies. The right histogram in Fig. 18 and Table 4 show that the masses of the YMC complexes range from $10^4 M_\odot$ in the nearby galaxies NGC 628 and NGC 6946 to $10^7 M_\odot$ in the distant galaxy NGC 7678; however, most of them have masses $10^5 - 10^6 M_\odot$.

Table 4 shows that the extinction in the studied star forming regions varies greatly, from 0 up to 3.5 mag. This result is in good agreement with the reddening measurements for the sample of 49 disc, halo and nuclear star clusters in M82 (Konstantopoulos et al. 2009).

The following physical parameters of the SF regions are presented in Table 4. Deprojected galactocentric distances in units of kpc and in units of isophotal radius, corrected for the Galactic extinction and inclination effects, are given in columns (2) and (3), respectively. Column (4) presents the estimated values of the light absorption A_V computed from the observed Balmer decrements. These values include Galactic extinctions $A(V)_{\text{Gal}}$. The equivalent widths, $EW(H\alpha)$, obtained in Gusev et al. (2012) and Gusev et al. (2013) are shown in column (5). The chemical abundances Z , estimated from spectroscopic observations (Gusev et al. 2012; Gusev et al. 2013) using the equations of Pilyugin & Mattsson (2011), are given in column (6). The estimated values of the nebular emission contribution in the B band are given in column (7). The ages, t , and masses, m , of the YMC complexes are shown in columns (8) and (9), respectively. The estimated diameters are presented in column (10). The structure of the SF regions is described in column (11). Lastly, the notes are given in column (12).

Note that the diameters of the SF regions in NGC 2336 presented in Table 4 are larger than those published in Gusev & Park (2003). In the present paper we estimate the diameter as the geometric mean of d_{max} and d_{min} , instead of d_{min} as in Gusev & Park (2003).

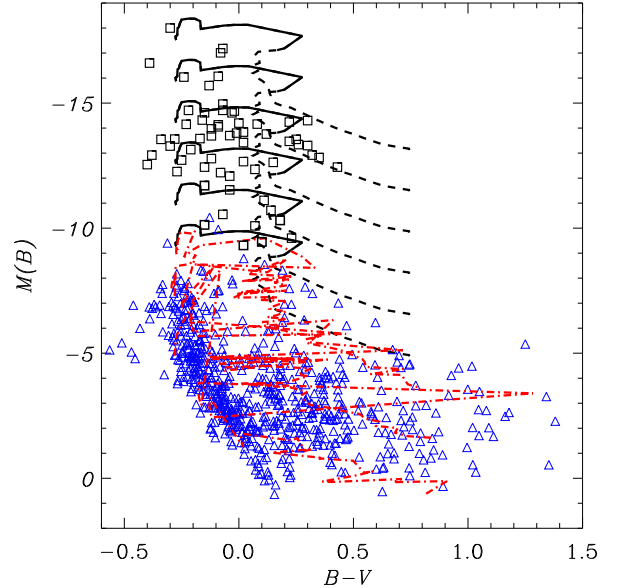


Figure 19. True colours and luminosities of YMC complexes (squares), compared with the *Standard* mode of SSP models (continuously populated IMF), and of OCs in the Milky Way (triangles), compared with the *Extended* SSP mode (randomly populated IMF). Only YMC complexes with estimated ages and masses are shown. In black we show the tracks of the *Standard* mode with an adopted characteristic metallicity of the studied YMCs of $Z = 0.012$, drawn in the age interval from 1 to 10 Myr as solid, and in the age interval from 10 Myr to 1.5 Gyr as dashed lines. The tracks were computed for the following masses of star clusters: $2 \cdot 10^7 M_\odot$, $4.4 \cdot 10^6 M_\odot$, $9.6 \cdot 10^5 M_\odot$, $2.1 \cdot 10^5 M_\odot$, $4.6 \cdot 10^4 M_\odot$, and $1 \cdot 10^4 M_\odot$. Grey dot-dashed lines show the *Extended* mode tracks for characteristic metallicity of OCs ($Z = 0.019$) computed for the $1 \cdot 10^4 M_\odot$, $9 \cdot 10^3 M_\odot$, $1.2 \cdot 10^3 M_\odot$, and $150 M_\odot$ in the age interval from 1 Myr to 9.8 Gyr.

7 COMPARISON OF EXTRAGALACTIC SF REGIONS AND MILKY WAY OPEN CLUSTERS IN THE INTEGRATED COLOUR-MAGNITUDE DIAGRAM

The currently accepted paradigm for star formation assumes that open clusters are born in a super cluster. They are not formed in isolation, but in stellar complexes born out of giant molecular clouds. As the giant molecular clouds disappear after the star formation is complete, they may seed the galactic disc with families of young clusters (cluster complexes). These families gradually disperse to become individual clusters and, eventually, field populations. We investigate the existence of the evolutionary relation between YMC complexes embedded in giant H II regions and open clusters using a comparative analysis of the evolution of the integrated photometric parameters for the studied YMC complexes and the open star clusters in our Galaxy in a colour-magnitude diagram.

Fig. 19 shows the colour-magnitude diagram for the YMC complexes in the studied galaxies and for the Galactic open clusters (OCs). We use a catalogue of 650 OCs and compact associations in the Milky Way (Kharchenko et al. 2005a,b) that were identified in the All-Sky Compiled Catalogue of 2.5 million stars (ASCC-2.5) complete to $V \approx 11.5$ (Kharchenko 2001). The integrated absolute magnitudes and intrinsic colours of the OCs were estimated by Kharchenko et al. (2009). The true photometric quantities of the YMC complexes, unaffected by extinction and nebula emission, were estimated from the observed ones taking into account

the interstellar reddening and nebula emission contribution in photometric bands (see Sections 2 and 4).

Fig. 19 shows that the YMC complexes in the galaxies and the OCs in the Milky Way form a continuous sequence of luminosities/masses and colour/ages. This diagram shows a hypothetical colour–magnitude diagram that will be observed in remote galaxies when the depth of present day extragalactic surveys is increased approximately by 10 mag.

It is worth noting that the observed continuity exhibits the hierarchical properties of star formation but it is not connected with the properties of the YMCs themselves. The SF region can consist, in its brightest part, of several young massive stellar clusters (a YMC complex), which can be observed as a single object because of the weak spatial resolution at large distances. As we noted in Gusev et al. (2014), the multiple structure of the unresolved complex of YMCs does not affect their integrated brightness M_B and colour index $B - V$. One can estimate the number of the brightest Milky Way clusters (BMWC) required to reproduce the positions of the studied SF regions in the CMD. It is enough to move the BMWC up to $M_B \approx -15$ mag. A value of $\Delta M_B = -5$ mag corresponds to a luminosity excess of $L_{\text{YMC}}(B)/L_{\text{BMWC}}(B) \approx 100$, where $L_{\text{YMC}}(B)$ is the typical luminosity of our cluster complexes, and $L_{\text{BMWC}}(B)$ is the luminosity of the BMWC. The corresponding mass can be found with the help of the mass–luminosity ratio. The SSP models show that for young clusters ($\log t \leq 7$), the ratio $m_{\text{cl}}/L_V < 0.1$, both for standard and extended modes (see Fig. 12 in Piskunov et al. 2011). Since young clusters are brighter in B than they are in V , the ratio m_{cl}/L_B is even smaller than 0.1. Then the typical mass of a complex that emits the observed flux will be on the order of $10 m_{\text{BMWC}}$, i.e. our complexes may not contain more than 10 BMWC. Note that in the Solar Neighbourhood, one can identify many young complexes with sizes from 150–700 pc, containing tens of associations, star clusters, and H II regions (Efremov & Sitnik 1988). So we can conclude that the observed YMCs are comparable to what we know in the Solar Neighbourhood.

In Fig. 19, we show the *Standard* mode of SSP models with continuously populated IMF computed for high luminosity ($M_B < -9$, $m_{\text{cl}} > 10^4 M_\odot$ and age $t < 10$ Myr) YMC complexes in galaxies and the *Extended* mode of SSP models with randomly populated IMF, computed for relatively low luminosity Galactic OCs ($M_B > -9$, $50 M_\odot < m_{\text{cl}} < 10^4 M_\odot$ and $1 \text{ Myr} < t < 1 \text{ Gyr}$). The dispersion of the integrated colours of the YMC complexes in the galaxies is due to both colour measurement errors and the natural dispersion of their physical parameters (ages). A comparison with the models shows that the YMC complexes belong to the young area of models, with $t < 10$ Myr, while the OCs cover the area of the models with a wide age interval, from 1 Myr up to 1 Gyr. We excluded from Fig. 19 those SF regions for which the ages and masses were not obtained.

8 DISCUSSION

Our estimates of the physical parameters of the YMC clusters are based on the assumption $A(\text{gas}) = A(\text{stars})$. In Section 4 we discussed obvious cases where this condition is not valid. Whitmore et al. (2011) proposed an evolutionary classification scheme of YMCs based on *HST* observations of M83. They showed that in clusters with ages 1 – 4 Myr, the ionised gas is spatially coincident with the cluster stars. For these clusters, the condition $A(\text{gas}) = A(\text{stars})$ is satisfied. YMCs with ages ≈ 5 Myr and older

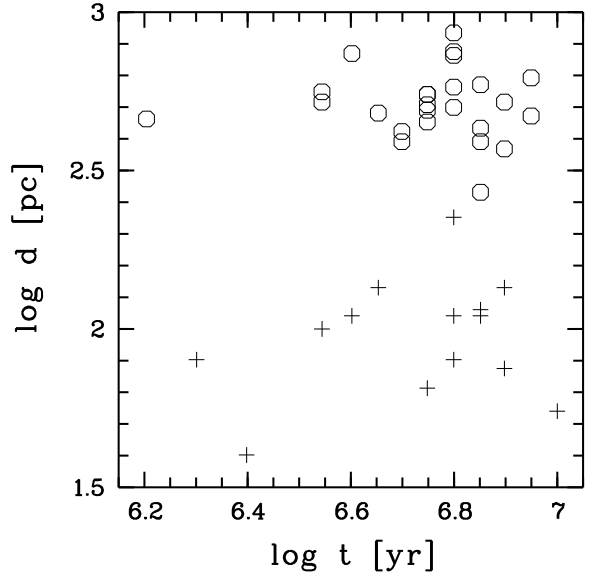


Figure 20. ‘Age–size’ diagram for SF regions in nearby (crosses) and distant (circles) galaxies. See the text for details.

have a large ionised gas bubble surrounding the cluster. The radius of the bubble is larger than 20 pc. In the nearby galaxies, such as NGC 628 and NGC 6946, the resolution of our observations ≈ 40 pc allows us to separate the gas and star clusters in space. Sometimes we can not use our spectroscopic data for the estimation of $A(\text{stars})$ for such objects (see Sections 4, 5, and Figs. 13, 15). However, for the majority of the SF regions older than 5 Myr, we can adequately estimate $A(\text{stars})$. YMCs with ages $\approx 4 - 5$ Myr have a small H II bubble surrounding the cluster. The radii of the bubbles are 7 – 20 pc (Whitmore et al. 2011). The stage of the partially embedded cluster when the cluster blows a gas bubble is quite short, about 1 Myr (Hollyhead et al. 2015). Our observations do not allow us to separate gas bubbles from star clusters. As a result, our values of $A(\text{stars})$ will be overestimated for these YMCs. This is indicated by a significant number of star clusters with an extremely blue $B - V$ colour index in NGC 6946 (Table 4, see the objects marked ‘6’ in the notes). Note that the ratio of the number of extremely blue YMCs to the number of YMCs with obtained ages and masses in the nearby galaxies NGC 628, NGC 6946, and NGC 7331 (12/29) is close to the ratio of the number of partially embedded YMCs to the number of embedded and exposed YMCs (16/50) according to Hollyhead et al. (2015).

YMC complexes in more distant galaxies are conglomerates of star clusters, associations, and ionised gas bubbles. The effects of the spatial distribution of star groupings and H II gas bubbles are smoothed for the distant SF regions. The averaged gas and star extinctions are approximately equal to each other. Only a few objects in the distant galaxies have colour indices outside the limits of the model tracks (Tables 4, A1).

As seen from the evolutionary tracks in Figs. 16 and 17, the colours of YMC clusters vary slightly during the first 3 – 4 Myr of a SF region’s life. The ages of SF regions younger than 4 Myr can be estimated with low accuracy using our technique. The colours of YMC clusters with ages from 4 to 8 Myr stringently depend on the age (Fig. 16). The age of these SF regions can be estimated with considerable accuracy. The errors of age depend only on the errors of the true colour indices.

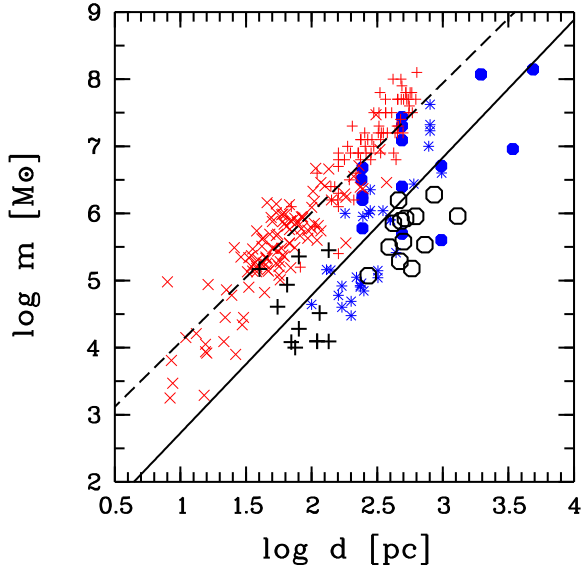


Figure 21. The ‘size–mass’ diagram for SF regions of our sample (symbols are the same as in Fig. 20), YMC complexes in very distant ($z \sim 1.5$) galaxy Sp 1149 (dark filled circles) and cluster complexes in the local galaxies (dark stars) by Adamo et al. (2013), GMCs from Bolatto et al. (2008) (grey crosses ‘x’) and Wei, Keto & Ho (2012) (grey crosses ‘+’). The solid line is a linear fit, computed for local and high- z YMC complexes in Adamo et al. (2013). The dashed line is a linear fit, computed for GMCs from the Bolatto et al. (2008) sample. See the text for details.

The photometric ages of the SF regions’ population younger than 10 Myr are consistent with the maximum lifetime of giant H II regions and the age distribution of 45 star forming complexes, fitted with the simultaneous star formation models (SSF model), with a mean age $4.5^{+4.5}_{-2.5}$ Myr (Sakhibov & Smirnov 2000). Note that Sakhibov & Smirnov (2000) used grids for both models: the simultaneous star formation model (SSF) and the infinite continuous star formation model (CSF) for the confrontation of the intrinsic colour indices of 113 star forming complexes in 22 spiral and irregular galaxies with the predicted colour indices. The star forming complexes, fitted with infinite continuous star formation models (CSF model), show a mean age 10^{+30}_{-8} Myr. The spread in the age of 14 intense starbursts in irregular and compact galaxies, estimated by Mas-Hesse & Kunth (1999), is narrower (2.5 – 6.5 Myr).

The combination of broadband multicolour photometry and emission spectra of SF regions, used in current research, provides age estimations only for young massive cluster complexes with ages less than 10 Myr. Konstantopoulos et al. (2009) derived the ages of 44 bright isolated star clusters in the range 30 Myr to 270 Myr, using absorption spectra combined with photometric data.

Modern high resolution studies suggest that SF regions present an age spread comparable to the size of the regions (Bastian et al. 2005; Whitmore et al. 2011; Kim et al. 2012). Thus, the size of an H II region is a function of the age of the stellar population. The resolution of our photometric observations does not allow us to explore the ‘age–size’ dependence for individual star clusters. The sizes of the H II regions beginning from 40 pc depend weakly on the age of the stellar population (see Fig. 4 (top) in Whitmore et al. 2011, for instance). A different situation is observed for star associations. The ‘age–size’ relation for star associations was first established by Efremov & Elmegreen (1998) for star groupings in LMC and was later confirmed in

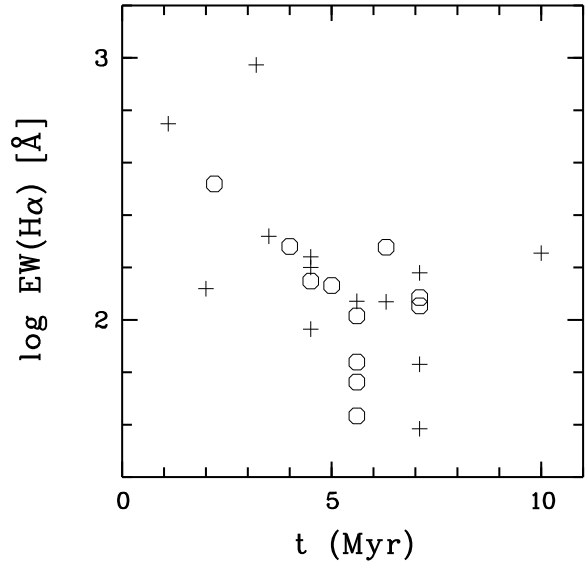


Figure 22. The ‘age–EW(H α)’ diagram for the studied SF regions. Symbols are the same as in Fig. 20. See the text for details.

Sakhibov & Smirnov (2001) for SF regions in other galaxies. Associations in the Milky Way and in other galaxies inside and outside the Local Group also show correlations between age and size (see Fig. 8 in Portegies Zwart et al. 2010).

Fig. 20 shows the dependence between the age and the size of the studied SF regions. In order to make a homogeneous sample, we excluded multiple (double, triple, and complex) objects from the graph (see column (11) in Table 4). As seen from the figure, the SF regions (stellar associations) in the nearby galaxies NGC 628, NGC 6946, and NGC 7331 satisfy the ‘age–size’ relation. Larger star associations are older. Single YMCs have smaller sizes. A possible example of such a YMC is the relatively old and compact SF region No. 18 in NGC 6946, with an age of 10 Myr and diameter of 55 pc.

The sizes of the large SF regions in the distant galaxies (large YMC complexes) do not correlate with age (Fig. 20). Obviously, all of them have a complex structure and contain a conglomerate of numerous YMCs and associations. Each cluster/association expands with age inside the complex, but the size of the complex depends basically on the physical parameters of the surrounding interstellar matter and the magnetic field (Elmegreen, Elmegreen & Leitner 2003; Elmegreen et al. 2003; Gusev & Efremov 2013).

Larson (1981) found a correlation between the sizes and the masses of giant molecular clouds (GMCs), $m \sim d^2$. This correlation has been repeatedly confirmed (see, e.g., Hopkins 2012). As is known, YMC complexes are the direct descendants of GMCs. As a result, the mass–size relation for YMC complexes was found to be close to that of GMCs (see Adamo et al. 2013, and references therein). Adamo et al. (2013) found a relation $m \sim d^{2.0 \pm 0.3}$ for YMC complexes and $m \sim d^{1.9 \pm 0.1}$ for GMCs from the sample of Bolatto et al. (2008). These relations are plotted in Fig. 21.

We examined the dependence between the sizes and the masses for the studied SF regions (Fig. 21). As in Fig. 20, we excluded multiple objects from the graph. In addition, we excluded SF regions with errors of mass estimation larger than $\pm 20\%$. As can be seen in the figure, there is no correlation between the masses and the ages for the SF regions in the nearby galaxies. Among

the objects in NGC 628 and NGC 6946 which have diameters $\sim 60 - 130$ pc, we observe both compact regions with masses $\sim 10^5 M_\odot$ and doughy regions with masses $\sim 10^4 M_\odot$. Nevertheless, they follow the general relation for YMCs (Fig. 21). One of the YMCs (No. 13 in NGC 6946) is located in the area occupied by GMCs. Note that this cluster is the core of a larger complex and it is the youngest object of our sample among the regions with confident estimates of ages (2.5 ± 0.5 Myr).

We did not find a very strong correlation between the sizes and the masses for the YMC clusters in the distant galaxies (Fig. 21). Nevertheless, they follow the relation $m \sim d^2$ for YMC complexes, as well as data from Adamo et al. (2013). Obviously, the correlation which is observed for YMC complexes is a relic of the ‘size–mass’ dependence for their ancestors, the GMCs. The vertical offset between the GMCs and the YMC complexes in the diagram could be due to the efficiency of star formation: only a fraction of the gas in the GMCs will form stars (Bastian et al. 2005; Adamo et al. 2013).

The equivalent widths of the $H\alpha$ and $H\beta$ emission lines can be used to infer the ages of YMC clusters (e.g., Copetti, Pastoriza & Dottori 1986; Alonso-Herrero et al. 1996; Reines, Johnson & Hunt 2008; Reines et al. 2010). Starburst99 evolutionary models show that $EW(H\alpha)$ in H II regions falls from $> 1000\text{\AA}$ in the youngest YMCs to $\approx 30 - 40\text{\AA}$ in the regions with an age of 10 Myr (Reines et al. 2010). The dependence between $EW(H\alpha)$ and the ages of the studied SF regions is shown in Fig. 22. In contrast to the samples in Fig. 20, 21, we included objects of any structure in the figure, but excluded objects with errors of $EW(H\alpha)$ larger than $\pm 10\%$. Fig. 22 shows that the SF regions follow the Starburst99 evolutionary models, however several objects of intermediate age (5–7 Myr) have lower $EW(H\alpha)$ than predicted by the models. There are no differences between the YMC/star associations in the nearby galaxies and those of the YMC/star complexes in the distant galaxies in the distribution in the ‘ t – $EW(H\alpha)$ ’ diagram. Note only a larger dispersion in the distribution of clusters/associations (crosses) compared to complexes (circles) in Fig. 22.

9 CONCLUSIONS

In this paper, we have presented a combination of spectroscopic and photometric studies of the disc cluster population in seven spiral galaxies. Our primary goal was to derive spectroscopic information on star forming regions (extinction, chemical abundance, relative contributions of nebular continuum and emission lines to the total observed flux) and photometric information on young massive clusters (true colour, luminosity, mass, age) embedded in SF regions. Combining the information from spectroscopy and imaging, we found that disc clusters in external galaxies and open clusters in the Milky Way show a uniform sequence (evolutionary/mass).

We summarise the following conclusions.

1. Cluster reddening ranges from 0 to 3 mag in the studied spirals, which is in good agreement with the spectroscopic reddening estimations by Konstantopoulos et al. (2009) for 44 isolated disc clusters in the M82. Accounting for the light extinction, based on independent spectroscopic observations, provides photometric ages of young massive clusters (cluster complexes) embedded in SF regions within 10 Myr.

2. The relative contributions of the nebular continuum and the emission lines to the total observed flux for most of the star forming regions are lower than 40% of the total fluxes of the SF regions, with a mean value of $\approx (20 - 22)\%$ in the B and V bands (Fig. 11).

This means that the impact of nebular emission on integrated broadband photometry is not greater than the observational (photometric + spectroscopic) errors.

3. Estimates of ages for 57 and masses for 63 of 102 YMC complexes embedded in H II regions were obtained. The photometric ages of the SF regions population younger than 10 Myr are consistent with the maximum lifetime of giant H II regions.

4. The derived masses of YMCs range from $10^4 M_\odot$ in the nearby galaxy NGC 628 to $10^7 M_\odot$ in the most distant NGC 7678. More than 80% of the YMC complexes have masses between $10^5 M_\odot$ and $10^6 M_\odot$. The lowest mass estimate of $10^4 M_\odot$ for the objects in NGC 628 and NGC 6946 belongs to the mass interval of the youngest Galactic open clusters. This is an argument for a uniform evolutionary sequence of extragalactic star forming regions and Galactic OCs.

5. Extragalactic young massive clusters and open star clusters in the Milky Way represent a single evolutionary sequence of objects at different stages of their evolution. The observed YMCs are comparable to what we know in the Solar Neighbourhood.

ACKNOWLEDGMENTS

We are grateful to the referee for constructive comments. The authors acknowledge the use of the HyperLeda database (<http://leda.univ-lyon1.fr>), the NASA/IPAC Extragalactic Database (<http://ned.ipac.caltech.edu>), and the Padova group online server CMD (<http://stev.oapd.inaf.it>). This study was supported by the Russian Science Foundation (project no. 14–22–00041).

REFERENCES

- Adamo A., Östlin G., Bastian N., Zackrisson E., Livermore R. C., Guaita L., 2013, *ApJ*, 766, 105
- Alonso-Herrero A., Aragón-Salamanca A., Zamorano J., Rego M., 1996, *MNRAS*, 278, 417
- Artamonov B. P., Bruevich V. V., Gusev A. S., 1997, *Astron. Rep.*, 41, 577
- Artamonov B. P., Badan Y. Y., Bruevich V. V., Gusev A. S., 1999, *Astron. Rep.*, 43, 377
- Artamonov B. P. et al., 2010, *Astron. Rep.*, 54, 1019
- Bastian N., Gieles M., Efremov Y. N., Lamers H. J. G. L. M., 2005, *A&A*, 443, 79
- Belley J., Roy J.-R., 1992, *ApJS*, 78, 61
- Bertelli G., Bressan A., Chiosi C., Fagotto F., Nasi E., 1994, *A&AS*, 106, 275
- Bessell M. S., 1990, *PASP*, 102, 1181
- Bolatto A. D., Leroy A. K., Rosolowsky E., Walter F., Blitz L., 2008, *ApJ*, 686, 948
- Bressan A., Marigo P., Girardi L., Salasnich B., Dal Cero C., Rubele S., Nanni A., 2012, *MNRAS*, 427, 127
- Brown R. L., Mathews W. G., 1970, *ApJ*, 160, 939
- Bruevich V. V., Gusev A. S., Ezhkova O. V., Sakhibov F. K., Smirnov M. A., 2007, *Astron. Rep.*, 51, 222
- Copetti M. V. F., Pastoriza M. G., Dottori H. A., 1986, *A&A*, 156, 111
- Dinerstein H. L., 1990, in *The Interstellar Medium in Galaxies*, eds. H. A. Thronson (Jr.) and J. M. Shull (Dordrecht: Kluwer), 257
- Epinat B., Amram P., Marcelin M., 2008, *MNRAS*, 390, 466
- Efremov Y. N., Elmegreen B., 1998, *MNRAS*, 299, 588
- Efremov Y. N., Sitnik T. G., 1988, *Soviet Astronomy Letters*, 14, 347
- Elmegreen B. G., Efremov Y. N., 1996, *ApJ*, 466, 802
- Elmegreen B. G., Elmegreen D. M., Leitner S. N., 2003, *ApJ*, 590, 271
- Elmegreen B. G., Elmegreen D. M., Salzer J. J., Mann H., 1996, *ApJ*, 467, 579

Elmegreen B. G., Leitner S. N., Elmegreen D. M., Cuillandre J.-C., 2003b, *ApJ*, 593, 333

Gieles M., Portegies Zwart S. F., 2011, *MNRAS*, 410, L6

Girardi L., Bressan A., Bertelli G., Chiosi C., 2000, *A&AS*, 141, 371

Gusev A. S., 2006a, *Astron. Rep.*, 50, 167

Gusev A. S., 2006b, *Astron. Rep.*, 50, 182

Gusev A. S., Efremov Y. N., 2013, *MNRAS*, 434, 313

Gusev A. S., Park M.-G., 2003, *A&A*, 410, 117

Gusev A. S., Egorov O. V., Sakhibov F., 2014, *MNRAS*, 437, 1337

Gusev A. S., Guslyakova S. A., Novikova A. P., Khramtsova M. S., Bruevich V. V., Ezhkova O. V., 2015, *Astron. Rep.*, 59, 899

Gusev A. S., Pilyugin L. S., Sakhibov F., Dodonov S. N., Ezhkova O. V., Khramtsova M. S., 2012, *MNRAS*, 424, 1930

Gusev A. S., Piskunov A. E., Sakhibov F. K., Kharchenko N. V., 2009, *Astron. Lett.*, 35, 679

Gusev A. S., Sakhibov F. H., Dodonov S. N., 2013, *Astr. Bull.*, 68, 40

Hollyhead K., Bastian N., Adamo A., Silva-Villa E., Dale J., Ryon J. E., Gazak Z., 2015, *MNRAS*, 449, 1106

Holtzman J. A., Burrows C. J., Casertano S., Hester J. J., Trauger J. T., Watson A. M., Worthey G., 1995, *PASP*, 107, 1065

Hopkins P. F., 2012, *MNRAS*, 423, 2016

Izotov Y. I., Thuan T. X., Lipovetsky V. A., 1994, *ApJ*, 435, 64

Kaplan S. A., Pikelner S. B., 1979, *The physics of the interstellar medium*. Nauka, Moscow, p. 592 (In Russian)

Kennicutt R. C., Hodge P. W., 1980, *ApJ*, 241, 573

Kharchenko N. V., 2001, *Kinematika Fizika Nebesnykh Tel*, 17, 409

Kharchenko N. V., Piskunov A. E., Röser S., Schilbach E., Scholz R.-D., 2005a, *A&A*, 438, 1163

Kharchenko N. V., Piskunov A. E., Röser S., Schilbach E., Scholz R.-D., 2005b, *A&A*, 440, 403

Kharchenko N. V., Piskunov A. E., Röser S., Schilbach E., Scholz R.-D., Zinnecker H., 2009, *A&A*, 504, 681

Kim et al., 2012, *ApJ*, 753, 26

Konstantopoulos I. S., Bastian N., Smith L. J., Westmoquette M. S., Tranco G., Gallagher J. S., 2009, *ApJ*, 701, 1015

Landolt A. U., 1992, *AJ*, 104, 340

Lang K. R., 1978, *Astrophysical Formulae. A Compendium for the Physicist and Astrophysicist*. Springer-Verlag, Berlin, Heidelberg, New York, p. 783

Larsen S. S., 1999, *A&AS*, 139, 393

Larsen S. S., 2004, *A&A*, 416, 537

Larson R. B., 1981, *MNRAS*, 194, 809

Maíz-Apellániz J., Mas-Hesse J. M., Muñoz-Tuñón C., Vílchez J. M., Castañeda H. O., 1998, *A&A*, 329, 409

Marigo P., Girardi L., 2007, *A&A*, 469, 239

Marigo P., Girardi L., Bressan A., Groenewegen M. A. T., Silva L., Granato G. L., 2008, *A&A*, 482, 883

Mas-Hesse J. M., Kunth D., 1999, *A&A* 349, 765

Osterbrock D. E., 1989, *Astrophysics of gaseous nebulae and active galactic nuclei*. University Science Books, Mill Valley, CA, p. 422

Paturel G., Petit C., Prugniel Ph., Theureau G., Rousseau J., Brouty M., Dubois P., Cambresy L., 2003, *A&A*, 412, 45

Pilyugin L. S., Mattsson L., 2011, *MNRAS*, 412, 1145

Piskunov A. E., Kharchenko N. V., Schilbach E., Röser S., Scholz R.-D., Zinnecker H., 2009, *A&A*, 507, L5

Piskunov A. E., Kharchenko N. V., Schilbach E., Röser S., Scholz R.-D., Zinnecker H., 2011, *A&A*, 525, A122

Portegies Zwart S. F., McMillan S. L. W., Gieles M., 2010, *ARA&A*, 48, 431

Reines A. E., Johnson K. E., Hunt L. K., 2008, *AJ*, 136, 1415

Reines A. E., Nidever D. L., Whelan D. G., Johnson K. E., 2010, *ApJ*, 708, 26

Sakhibov F., Smirnov M. A., 1990, *Soviet Astronomy*, 34, 236

Sakhibov F., Smirnov M. A., 2000, *A&A*, 354, 802

Sakhibov F., Smirnov M. A., 2001, *Astron. Rep.*, 45, 1

Sakhibov F., Gusev A. S., Kharchenko N. V., Piskunov A. E., 2010, *Proc. IAU Symp.* 266, 522

Scalo J. M., 1986, *Fundamentals of Cosmic Physics*, 11, 1

Wei L. H., Keto E., Ho L. C., 2012, *ApJ*, 750, 136

Whitmore B. C. et al., 2011, *ApJ*, 729, 78

APPENDIX A:

Table A1. True magnitudes and colours of SF regions.

NGC	No.	M_B	ΔM_B	$U - B$	$\Delta(U - B)$	$B - V$	$\Delta(B - V)$	$V - R$	$\Delta(V - R)$	$V - I$	$\Delta(V - I)$
628	1	-11.40	0.912	-1.11	0.180	-0.40	0.229	-0.18	0.153	-0.08	0.318
628	2	-11.70	0.715	-0.26	0.153	-0.15	0.181	0.05	0.122	0.12	0.251
628	3	-9.31	0.640	-1.02	0.137	0.02	0.190	0.74	0.138	0.92	0.272
628	4	-10.13	0.932	-0.69	0.200	-0.15	0.249	0.04	0.183	0.09	0.368
628	8	-9.45	0.348	-0.42	0.074	0.10	0.092	0.59	0.064	0.79	0.136
628	10	-10.31	0.658	-0.50	0.132	0.18	0.167	0.30	0.113	0.44	0.231
783	1	-12.35	0.543	-0.39	0.240	0.07	0.282	0.40	0.227	0.68	0.344
783	3	-14.68	0.274	-0.11	0.068	-0.02	0.101	-0.32	0.100	0.11	0.167
783	4	-14.96	0.632	-0.63	0.162	-0.07	0.213	-0.05	0.164	0.08	0.272
783	5	-13.84	0.302	-0.30	0.083	0.02	0.098	-0.32	0.095	0.02	0.156
2336	1	-13.34	0.454	-0.78	0.140	0.26	0.145	0.20	0.115	0.25	0.203
2336	2	-13.76	0.255	-0.29	0.093	0.12	0.085	0.26	0.056	0.39	0.107
2336	3	-14.15	0.501	-0.82	0.145	-0.23	0.179	0.01	0.151	0.15	0.234
2336	4	-14.24	0.295	-0.87	0.141	0.22	0.152	0.29	0.130	0.36	0.210
2336	5	-12.92	0.960	-0.69	0.245	0.32	0.275	0.38	0.197	0.40	0.388
2336	7	-12.63	0.481	-0.79	0.165	0.15	0.149	0.51	0.111	0.58	0.204
2336	8	-13.55	0.207	-0.36	0.067	0.25	0.068	0.17	0.061	0.29	0.107
2336	10	-14.61	0.175	-0.81	0.071	-0.15	0.073	-0.07	0.064	0.10	0.114
2336	11	-14.05	0.445	-1.23	0.164	-0.09	0.156	-0.03	0.112	0.12	0.205
2336	12	-14.71	0.811	-0.74	0.244	-0.07	0.244	0.08	0.180	0.12	0.340
2336	13	-16.60	0.255	-1.35	0.083	-0.39	0.085	-0.15	0.066	-0.06	0.107
2336	14	-14.32	0.192	-1.00	0.085	-0.16	0.087	-0.06	0.078	0.16	0.131
2336	15	-12.82	0.445	-0.44	0.150	0.35	0.159	0.26	0.114	0.30	0.222
2336	16	-13.42	0.267	-0.21	0.183	0.02	0.187	-0.01	0.174	0.21	0.225
2336	17	-15.70	0.143	-0.67	0.045	-0.13	0.054	-0.06	0.039	0.23	0.083
2336	20	-14.20	0.396	-1.08	0.119	0.00	0.129	-0.40	0.108	-0.14	0.185
2336	21	-12.44	0.388	-0.38	0.164	0.43	0.172	0.13	0.174	0.27	0.286
2336	24	-13.97	0.783	-1.05	0.228	-0.12	0.228	-0.24	0.166	-0.09	0.310
2336	25	-14.61	0.509	-1.09	0.140	-0.03	0.156	-0.24	0.116	-0.15	0.224
2336	26	-13.70	0.970	-1.23	0.235	-0.04	0.285	-0.39	0.217	0.00	0.388
2336	27	-13.80	0.725	-0.57	0.183	-0.01	0.221	-0.03	0.172	0.05	0.311
6217	2	-16.04	0.942	-1.16	0.210	-0.24	0.279	0.05	0.213	0.06	0.378
6946	3	-9.60	1.028	-0.95	0.231	0.23	0.302	-0.16	0.222	0.04	0.437
6946	5	-10.09	0.522	-0.38	0.225	0.07	0.309	0.00	0.285	0.05	0.435
6946	6	-13.14	0.207	-0.90	0.047	-0.21	0.058	-0.17	0.041	-0.07	0.077
6946	8	-11.11	0.217	-0.38	0.057	0.11	0.078	0.10	0.081	0.13	0.127
6946	9	-13.28	0.151	-0.91	0.037	-0.30	0.054	0.00	0.042	0.23	0.078
6946	10	-12.78	0.217	-0.84	0.057	-0.12	0.068	-0.16	0.051	-0.05	0.087
6946	11	-12.22	0.207	-0.85	0.047	-0.08	0.068	0.08	0.051	0.32	0.117
6946	12	-13.56	0.179	-0.90	0.042	-0.28	0.051	-0.16	0.037	-0.03	0.078
6946	13	-12.72	0.217	-1.09	0.067	-0.25	0.088	-0.01	0.071	0.15	0.117
6946	15	-12.92	0.148	-1.06	0.047	-0.38	0.058	-0.08	0.051	0.28	0.087
6946	18	-10.71	0.179	-0.67	0.042	0.14	0.051	0.09	0.037	0.35	0.078
6946	26	-12.44	0.151	-0.85	0.037	-0.15	0.054	0.11	0.042	0.34	0.088
6946	28	-13.55	0.545	-0.80	0.111	-0.34	0.140	-0.23	0.095	-0.14	0.193
6946	29	-12.08	0.433	-0.67	0.100	-0.04	0.122	-0.11	0.087	0.08	0.174
6946	30	-13.58	0.123	-1.09	0.031	-0.17	0.047	0.08	0.028	0.40	0.059
6946	31	-10.55	0.245	-0.74	0.063	-0.07	0.085	-0.01	0.076	0.16	0.127
6946	32	-12.54	0.235	-1.08	0.063	-0.40	0.075	-0.34	0.056	-0.18	0.107
6946	34	-12.26	0.179	-0.96	0.052	-0.27	0.071	-0.13	0.057	0.02	0.108
6946	35	-14.16	0.489	-0.38	0.110	0.08	0.136	-0.19	0.096	-0.15	0.184
6946	36	-11.53	0.217	-0.47	0.067	-0.04	0.088	0.19	0.071	0.52	0.127
6946	37	-12.66	0.837	-0.70	0.174	0.02	0.228	-0.08	0.169	0.02	0.319
7331	3	-14.13	0.519	-0.76	0.150	-0.09	0.186	-0.11	0.176	-0.07	0.284
7331	4	-13.69	0.245	-0.97	0.063	-0.12	0.075	0.11	0.056	0.23	0.107
7678	2	-13.47	0.622	-0.70	0.162	0.22	0.203	-0.01	0.164	0.07	0.302
7678	3	-14.30	0.330	-0.18	0.088	0.30	0.115	0.24	0.089	0.34	0.166
7678	5	-13.30	0.565	-0.27	0.151	0.30	0.190	0.09	0.165	0.15	0.273
7678	6	-16.07	0.415	-0.64	0.104	-0.09	0.136	-0.05	0.112	0.01	0.195
7678	7	-17.18	0.151	-0.86	0.037	-0.07	0.044	-0.08	0.032	0.05	0.058
7678	8	-18.00	0.088	-1.18	0.031	-0.30	0.037	-0.22	0.028	0.04	0.059
7678	9	-14.71	0.227	-1.19	0.077	-0.22	0.108	0.10	0.101	0.36	0.187
7678	10	-17.01	0.179	-0.68	0.052	-0.08	0.061	-0.15	0.047	-0.04	0.088

This figure "MN-15-0973-MJ-Fig15.jpg" is available in "jpg" format from:

<http://arxiv.org/ps/1601.07470v1>